

Amount of intergalactic dust: constraints from distant supernovae and thermal history of intergalactic medium

Akio K. Inoue^{*†1} and Hideyuki Kamaya²

¹ *Department of Physics, Faculty of Science, Kyoto University, Sakyo-ku, Kyoto 606-8502, Japan*

² *Department of Astronomy, Faculty of Science, Kyoto University, Sakyo-ku, Kyoto 606-8502, Japan*

Submitted on October 1?, 2003

ABSTRACT

This paper examines the allowed amount of IG (intergalactic) dust, which is constrained by extinction and reddening of distant SNe and thermal history of IGM (intergalactic medium) affected by dust photoelectric heating. Based on the observational cosmic star formation history, we find an upper bound of χ , the mass ratio of the IG dust to the total metal in the Universe, as $\chi \lesssim 0.1$ for $10\text{\AA} \lesssim a \lesssim 0.1\mu\text{m}$ and $\chi \lesssim 0.1(a/0.1\mu\text{m})^{-1}$ for $0.1\mu\text{m} \lesssim a \lesssim 1\mu\text{m}$, where a is a characteristic grain size of the IG dust. This upper bound of $\chi \sim 0.1$ suggests that the dust-to-metal ratio in the IGM is smaller than the current Galactic value. The corresponding allowed density of the IG dust increases from $\sim 10^{-34} \text{ g cm}^{-3}$ at $z = 0$ to $\sim 10^{-33} \text{ g cm}^{-3}$ at $z \sim 1$, and keeps almost the value toward higher redshift. This causes IG extinction of $\lesssim 0.2 \text{ mag}$ at the observer’s B -band for $z \sim 1$ sources and that of $\lesssim 1 \text{ mag}$ for higher redshift sources. Furthermore, if $E(B - V) \sim 0.1 \text{ mag}$ at the observer’s frame against $z \gtrsim 1$ sources is detected, we can conclude that a typical size of the IG dust is $\lesssim 100 \text{\AA}$. The 2175\AA absorption feature of small graphite may be found as a local minimum at $z \sim 2.5$ in a plot of the observed $E(B - V)$ as a function of the source redshift. Finally, the IGM mean temperature at $z \lesssim 1$ can be still higher than 10^4 K , provided the size of the IG dust is $\lesssim 100 \text{\AA}$.

Key words: cosmology: theory — dust, extinction — intergalactic medium — quasars: absorption lines

1 INTRODUCTION

As long as there is dust between radiation sources and observers, the dust extinction and reddening¹ must be corrected if we want to realize the nature of the sources. We should examine how much extinction and reddening there are. The extinction property in the Galaxy is a well studied example (e.g., Draine & Lee 1984). Indeed, the dust infrared map of the Galaxy, which traces the dust amount in lines of sight, has been summarised in Burstein & Heiles (1982); Schlegel, Finkbeiner, & Davis (1998). Hence, with reasonable accuracy, we can correct the extinction by the Galactic dust. Although the dust distribution and properties in the external galaxies are not well known yet, we can correct the dust extinction in the galaxies by using some indicators of the extinction with some assumptions (e.g., Buat et al. 2002). How about the extinction by the intergalactic (IG) dust?

We have already known the fact that some metal elements exist in the Lyman α clouds even at redshift larger than 3 (e.g., Cowie et al. 1995; Telfer et al. 2002). It suggests that the dust grains also exist in the low-density intergalactic medium (IGM). Such diffuse IG dust causes the IG extinction and reddening, which may affect on our understanding of the Universe significantly. One might think that the IG dust amount is negligible because such a significant IG reddening is not reported in the previous studies (Takase 1972; Cheng, Gaskell, & Koratkar 1991; Riess et al. 1998; Perlmutter et al. 1999). However, the wavelength dependence of the IG extinction is quite uncertain. If it is gray as suggested by Aguirre (1999), a large extinction is possible with no reddening. Nobody can conclude that the IG dust is negligible because of no observable reddening.

Theoretically, it is predicted that metals synthesized in supernova (SN) explosions form into the dust grains in the cooling ejecta of SNe (Kozasa & Hasegawa 1987; Todini & Ferrara 2001; Nozawa et al. 2003; Schneider, Ferrara, & Salvaterra 2003). Recently, thermal emissions of such dust from two supernova remnants, Cas A and Kepler, are detected (Dunne et al. 2003; Mörtzell & Goobar 2003). In a very high- z universe, SNe of massive Population III stars formed in low mass halos, which are likely to be the main site of the first star formation, can disperse the produced metals into the IGM (Bromm, Yoshida, & Hernquist 2003). The

* E-mail:akinoue@scphys.kyoto-u.ac.jp

† JSPS Research Fellow

¹ In this paper, we call the total absolute amount of the absorption and scattering at a wavelength just *extinction*, and the differential extinction between two wavelengths *reddening*.

dust grains may be also dispersed into the IGM. Therefore, the IG dust grains may exist even in a $z \gtrsim 10$ universe (Elfgren & Désert 2003).

Extinction by the IG dust may affect on the determination of the cosmological parameters from observations of SNe. The observed dimming beyond the geometrical dimming in the empty space of distant ($z \simeq 0.5$) SNe, which is attributed to the cosmological constant (Riess et al. 1998; Perlmutter et al. 1999), can be reproduced by the gray IG extinction without the cosmological constant (Aguirre 1999). Goobar, Bergstöm, & Mörtzell (2002) show that the apparent brightening of the farthest SNe ($z = 1.7$; Riess et al. 2001) can be also explained by the gray IG extinction with zero cosmological constant if the dust-to-gas ratio in the IGM decreases properly with increasing redshift. Therefore, to know the amount of the IG dust is also important in the cosmological context.

The evidence of the IG dust should be imprinted in the cosmic microwave background (CMB) and infrared background because the dust emits thermal radiation in the waveband from the far-infrared to submillimetre (submm) (Rowan-Robinson, Negroponte, & Silk 1979; Wright 1981; Elfgren & Désert 2003). Although the *COBE* data provides us with only a rough upper bound on the IG dust (Loeb & Haiman 1997; Ferrara et al. 1999; Aguirre & Haiman 2000), the data of *WMAP* (Spergel et al. 2003) may be promising. The submm background radiation will give a more strict constraint on the IG dust (Aguirre & Haiman 2000).

Recently, we have proposed a new constraint on the IG dust amount by using thermal history of the IGM (Inoue & Kamaya 2003). Since the dust photoelectric heating is very efficient in the IGM (Nath, Sethi, & Shchekinov 1999), the theoretical thermal evolution of the IGM taking into account of the dust heating violates the observationally allowed temperature evolution if too much IG dust is input in the model. Hence, Inoue & Kamaya (2003) obtain an upper bound of the IG dust amount in order that the theoretical IGM temperature should be consistent with the observed one. The obtained upper bound of the dust-to-gas ratio in the IGM is 1% and 0.1% of the Galaxy owing to the IG grain size of $\sim 100 \text{ \AA}$ – $0.1 \text{ }\mu\text{m}$ and $\sim 10 \text{ \AA}$, respectively, at redshift of ~ 3 .

In this paper, with help of distant SNe observation, we extend our previous approach in order to discuss the upper bounds of the IG dust extinction and reddening. In the next section, we start from the cosmic star formation history (SFH) to specify the IG dust amount at each redshift. According to the assumed SFH, we can estimate IG dust extinction and reddening at each redshift theoretically. In section 3, we comment on observational constraints

from the extinction and reddening of distant SNe. In section 4, further constraints are presented by comparing theoretical and observational thermal histories of the IGM. Based on the allowed amount of the IG dust, we also discuss some implications from our results in section 5. The achieved conclusions are summarised in the final section.

Throughout the paper, we stand on a Λ -cosmology. That is, we constrain the amount of the IG dust in order that the IG dust should not affect on the determination of the cosmological parameters from distant SNe. This is why the flat universe is favored by results of CMB observations (Jaffe et al. 2001; Pryke et al. 2002; Spergel et al. 2003), whereas only the matter cannot make the flat universe (Percival et al. 2001). Furthermore, the recent observations of the X-ray scattering halo around high- z QSOs suggest too small amount of the IG dust to explain all amount of the dimming of the distant SNe (Paerels et al. 2002; Telis et al. 2002, but see also Windt 2002). Mörtzell & Goobar (2003) also reach the same conclusion by analyzing the observed colours of the SDSS (Sloan Digital Sky Survey) quasars. The following cosmological parameters are adopted: $H_0 = 70 \text{ km s}^{-1} \text{ Mpc}^{-1}$, $\Omega_M = 0.3$, $\Omega_\Lambda = 0.7$, and $\Omega_b = 0.04$.

2 STAR FORMATION HISTORY AND INTERGALACTIC DUST

To estimate the IG extinction and reddening theoretically, we must investigate production of dust at each redshift. Since dust is made of metals, a cosmological evolution of the metal amount should be specified. As metals are products of stellar evolution, therefore, we shall specify the cosmic SFH as a first step.

Since Madau et al. (1996), researches of the cosmic SFH are extensively performed. In Figure 1, we show observational star formation rates in a unit comoving density as a function of redshift. The cross and open symbols are estimated from the $H\alpha$ line and the rest-frame ultra-violet (UV) luminosities not corrected by the dust extinction. Hence these are lower limits. The filled-circles are estimated from the submm data. Due to the small statistics, the uncertainty of the submm data is rather large. In this paper, we adopt two models: low and high SFHs, which are shown in Figure 1 as solid and dashed curves, respectively. These SFHs are formulated as

$$\frac{\rho_{\text{SFR}}^*(z)}{0.1 M_\odot \text{ yr}^{-1} \text{ Mpc}^{-3}} = \begin{cases} \left(\frac{1+z}{2}\right)^{3.3} & (\text{for } z \leq 1) \\ \left(\frac{1+z}{2}\right)^{-1.5} & (\text{for } z > 1 \text{ low SFH}) \\ 1 & (\text{for } z > 1 \text{ high SFH}) \end{cases}, \quad (1)$$

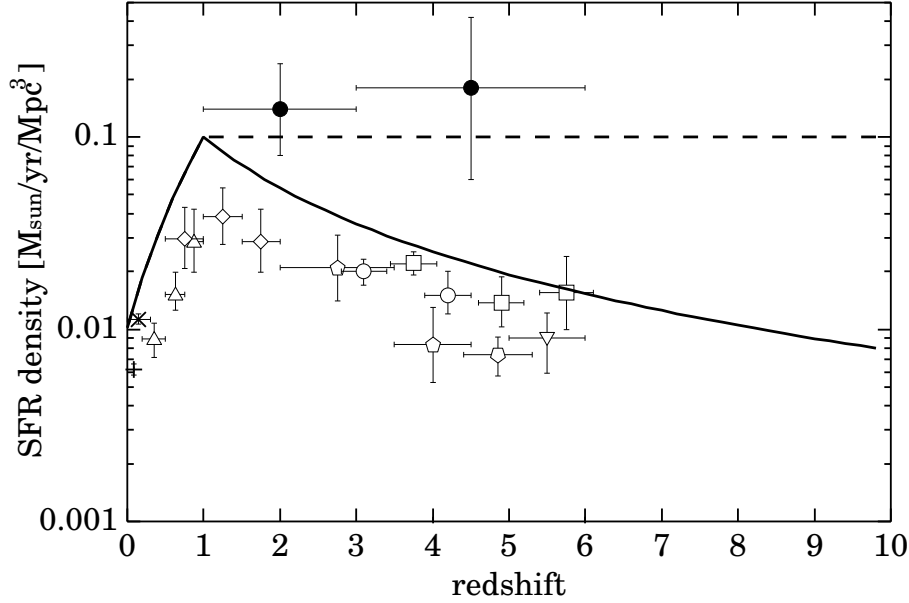


Figure 1. Cosmic star formation rate density as a function of redshift. The plotted points with error-bars are estimated from the $H\alpha$ data: cross (Gallego et al. 1995) and inclined cross (Tresse & Maddox 1998); from the rest-frame ultra-violet data: open-triangles (Lilly et al. 1996), open-diamonds (Connolly et al. 1997), open-pentagons (Madau, Pozzetti, & Dickinson 1998), open-circles (Steidel et al. 1999), open-squares (Giavalisco et al. 2003), open-inverse-pentagon (Iwata et al. 2003), open-inverse-triangle (Bouwens et al. 2003); and from the submillimetre data: filled-circles (Barger, Cowie, & Richards 2000). The solid and dashed curves are the models of low and high star formation histories, respectively.

where ρ_{SFR}^* is the star formation rate per unit comoving density.

Once a SFH is specified, the cosmic mean metallicity evolution is determined by:

$$Z(z) = \frac{y_Z}{\Omega_b \rho_{c,0}} \int_z^{z_S} \rho_{\text{SFR}}^*(z') \frac{dz'}{H(z')(1+z')}, \quad (2)$$

where y_Z is the produced metal mass fraction for a unit star forming mass, $\rho_{c,0}$ is the current critical density, z_S is the starting redshift of the cosmic star formation, and $H(z)$ is the Hubble constant at the redshift z . We have assumed y_Z to be a constant for simplicity. If the Salpeter initial mass function ($0.1\text{--}125 M_\odot$) is assumed, $y_Z = 0.024$ (Madau et al. 1996). We assume $z_S = 10$ in this paper. This does not affect on the results obtained in the following sections because the measure of time along the redshift is small in the high- z universe. Indeed, the cosmic metallicities in $z \lesssim 3$ for various z_S become nearly equal each other if $z_S \gtrsim 5$. In Figure 2, we show the mean cosmic metallicity as a function of redshift. In the figure, the metallicity range in the $\text{Ly}\alpha$ clouds observed by Songaila (2001) is overlaid. Although our theoretical estimate of metallicity is an average of the universe and the observed metallicity is that in the IGM, they show a good agreement with each other.

Let us introduce one parameter to describe the amount of the IG dust; the ratio of the IG dust mass to the total metal mass in the universe defined as

$$\chi \equiv \frac{\text{IG dust mass}}{\text{total metal mass}} = \frac{\mathcal{D}^{\text{IGM}}}{Z}, \quad (3)$$

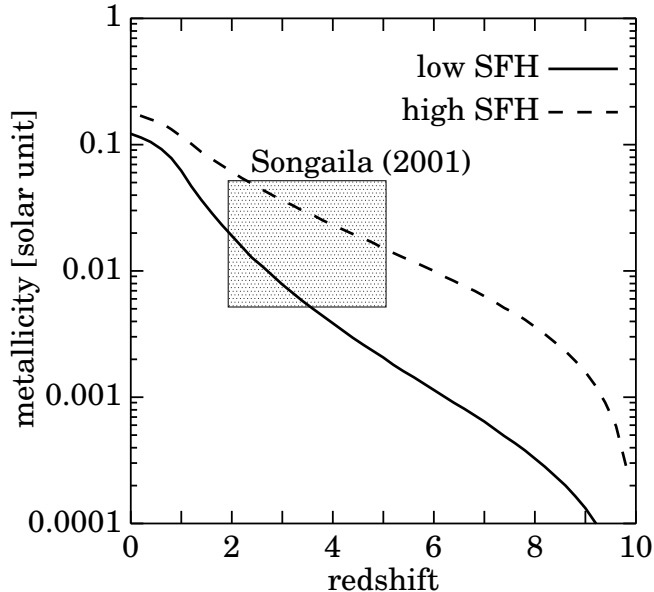


Figure 2. Mean cosmic metallicity evolution. The vertical axis is normalized by the Solar metallicity $Z_{\odot} = 0.02$. The solid and dashed curves are the cases of the low and high star formation histories, respectively. The starting redshift of the cosmic star formation is set to be $z_S = 10$. Metallicity range observed by Songaila (2001) is overlaid as the shaded square.

where \mathcal{D}^{IGM} is the dust-to-gas ratio in the IGM. In principle, this parameter is determined by the transfer mechanism of dust from galaxies into the IGM. Although some authors have tried this problem approximately (e.g., Ferrara et al. 1990, 1991; Aguirre et al. 2001), the results are not still conclusive. This is because we must solve problems of the magneto-radiation-hydrodynamics of dusty plasma finally. Here we approach the parameter χ by another way; we constrain the parameter by using the observational data of distant SNe (§3) and the thermal history of the IGM (§4). While the parameter χ may evolve along redshift, we treat it as a constant for simplicity. Hence, the obtained values of χ in the following sections are regarded as those averaged over redshift.

Dust model must also be specified. In this paper, we adopt the “graphite” and the “smoothed astronomical silicate” models by Draine & Lee (1984); Laor & Draine (1993); Weingartner & Draine (2001a), which can explain the interstellar dust properties in the Galaxy and the Magellanic clouds very well. Although there is no evidence that the IG dust is the same as the Galactic dust, we assume them as a working hypothesis. In Figure 3, the extinction efficiency factors of the grain models are displayed.

The grain size distribution in the IGM is also quite uncertain. Aguirre (1999) suggests a selection rule in the transfer of dust grains from the host galaxies into the IGM; the small grains are destroyed by the thermal sputtering process when the grains are transferred through the hot gas halo of the host galaxies. Indeed, this theoretical suggestion is very

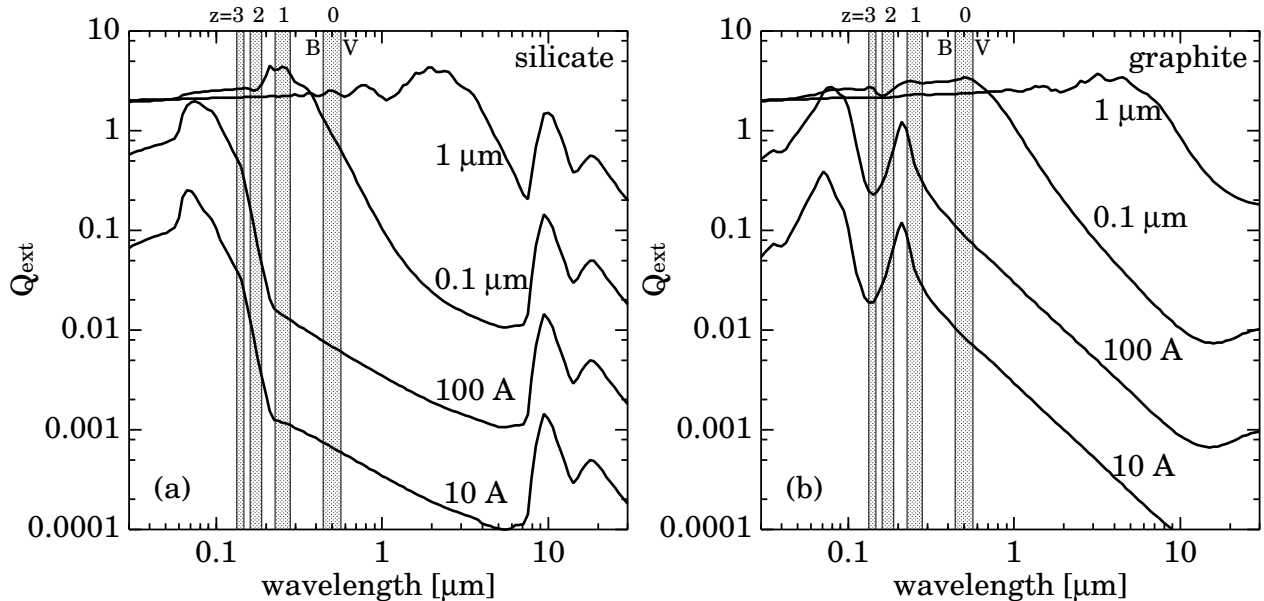


Figure 3. Extinction efficiency factors for (a) silicate grains and (b) graphite grains. Each solid curve is the model efficiency factor as a function of wavelength for the grain radius indicated near the curve. The data are taken from Draine & Lee (1984); Laor & Draine (1993); Weingartner & Draine (2001a). The shaded areas indicate the wavelength ranges between B and V -bands for the redshift $z = 0, 1, 2$, and 3 , respectively.

interesting to realize the gray dust model. However, we also examine the possibility of the small IG grain because the suggestion of the selection rule is not confirmed observationally at the moment. We hypothesise the delta function like size distribution for simplicity in the following sections. This means that the grain size in the current paper indicates a characteristic size of the IG dust (i.e. an averaged size by a certain way).

3 CONSTRAINT FROM OBSERVATIONAL DIMMING OF SUPERNOVAE

In this section, we constrain the amount of the IG dust by means of observational dimming of distant SNe. According to Riess et al. (2001), the dimming of SNe at $z \sim 0.5$ is $\sim 0.2 \pm 0.1$ mag against the empty universe. Our policy is that the IG dust extinction does not affect the interpretation of the cosmological constant. Thus, we attribute the 0.2 mag dimming of SNe at $z \sim 0.5$ to the cosmological constant and consider the remaining uncertainty of 0.1 mag to be caused by the IG extinction. Although the cosmological dimming does not depend on the observed wavelength, the remaining uncertainty may be depend on the wavelength if it is caused by the IG extinction. As the distant SNe are observed in B and V -bands and B -band provides a slightly more strict constraint than V -band, we regard the upper limit of 0.1 mag as that in the B -band. In addition, Perlmutter et al. (1999) report that the difference of the

observed reddening between the local and distant SNe is $\langle E(B-V) \rangle_{z=0.5} - \langle E(B-V) \rangle_{z=0.05} = 0.002 \pm 0.03$ mag. Although there seems to be no systematic difference, we can still consider the absolute value of the colour excess by the IG dust less than 0.03 mag. In summary, the upper limits of the IG extinction and reddening from observations of distant SNe at $z \sim 0.5$ are $A_{B,z=0.5}^{\text{IGM}} = 0.1$ mag and $|E(B-V)_{z=0.5}^{\text{IGM}}| = 0.03$ mag.

Suppose an observer who observes a source with a redshift of z at a wavelength of λ_{obs} in his/her rest frame. The amount of the IG extinction is given by

$$\frac{A_{\lambda_{\text{obs}}}^{\text{IGM}}(z)}{\text{mag}} = 1.086\pi a^2 \int_0^z Q\left(a, \frac{\lambda_{\text{obs}}}{1+z'}\right) n_{\text{d}}^{\text{IGM}}(z') \frac{c dz'}{(1+z')H(z')}, \quad (4)$$

where a is the grain radius, Q is the extinction efficiency factor, c is the light speed, and $n_{\text{d}}^{\text{IGM}}$ is the IG grain number density in a unit physical volume, which is

$$n_{\text{d}}^{\text{IGM}}(z) = \frac{\chi \Omega_{\text{b}} \rho_{\text{c},0} (1+z)^3 Z(z)}{4\pi a^3 \varrho/3}, \quad (5)$$

where $\varrho (= 2 \text{ g cm}^{-3})$ is the grain material density. In Figure 4, we show the amount of the IG extinction divided by χ for a source with $z = 0.5$ as a function of the assumed grain size. While the results for low SFH is depicted in the figure, the extinction amount for the high SFH case is only a factor of about 1.5 larger than that of the low SFH case. The extinction amount is independent of the grain size as long as $2\pi a < \lambda$. This is because (1) the extinction efficiency factor, Q_{ext} , is proportional to the grain size, a , linearly; (2) the number density of the grain has a dependence of a^{-3} for a fixed dust mass; and (3) the extinction cross section ($= Q_{\text{ext}} \pi a^2$) is proportional to a^3 . On the other hand, Q_{ext} becomes constant (almost 2) when $2\pi a > \lambda$, so that the extinction cross section is determined by mainly the geometrical one which is proportional to a^2 . When $2\pi a \sim \lambda$, grains interact with photons the most effectively, so that the amount of extinction shows a peak in both panels of figure 4.

We shall remember the observational constraints of $A_{B,z=0.5}^{\text{IGM}} \leq 0.1$ mag and $|E(B-V)_{z=0.5}^{\text{IGM}}| \leq 0.03$ mag. Hence, we can obtain the upper bound of χ via Eq.(4) or figure 4, which is shown in Figure 5. The solid and dotted curves indicate the upper bounds of χ based on $A_{B,z=0.5}^{\text{IGM}} = 0.1$ mag and $|E(B-V)_{z=0.5}^{\text{IGM}}| = 0.03$ mag, respectively. The thick and thin curves denote the cases of low and high SFHs, respectively. We find that, for both grain types, the upper bound of χ is $\sim 0.1 (0.1 \mu\text{m}/a)$ for $0.1 \mu\text{m} \lesssim a \lesssim 1 \mu\text{m}$. While we have no constraint of χ for the small ($a \lesssim 100 \text{ \AA}$) silicate grain (panel [a]), the upper bound of χ is ~ 0.1 when $a \lesssim 100 \text{ \AA}$ for the graphite case (panel [b]). This difference is caused by the different optical properties between graphite and silicate; small silicate is more transparent

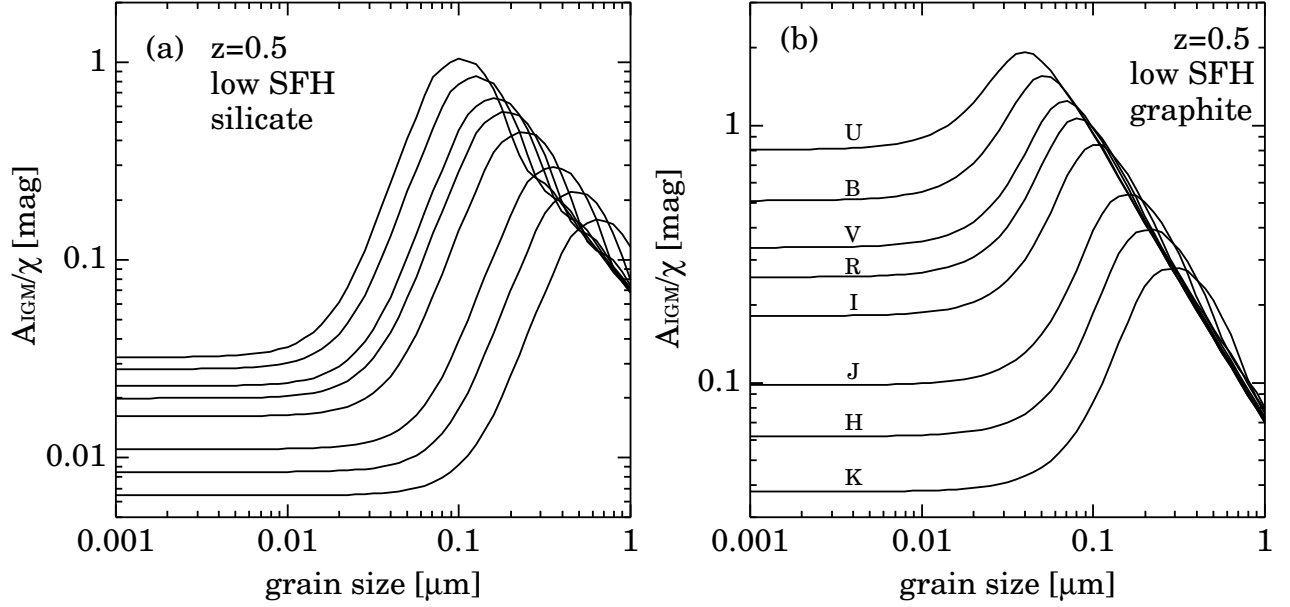


Figure 4. Intergalactic extinction in various bands against a source with the redshift $z = 0.5$ as a function of the IG grain size. The vertical axis is divided by the parameter χ , which is defined by equation (3). The panels (a) and (b) are the cases of silicate and graphite, respectively. The star formation history assumed is the lower case shown in Figure 1. The solid curves indicate the extinction amount in the U , B , V , R , I , J , H , and K bands from top to bottom.

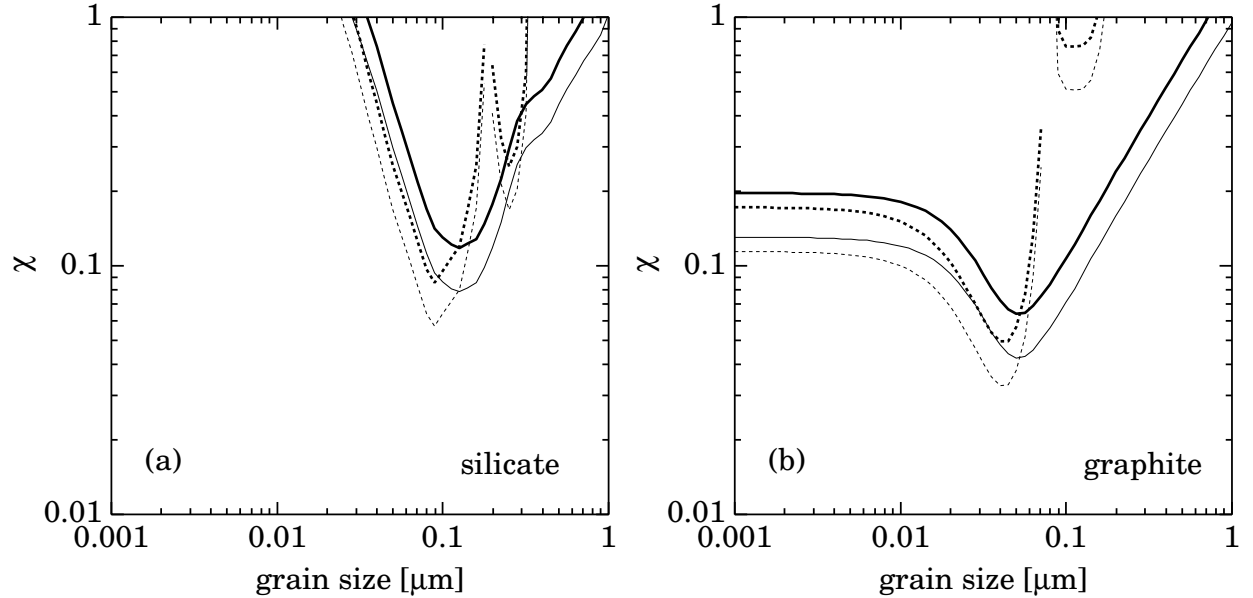


Figure 5. Upper boundary of mass ratio of the intergalactic dust to the total metal, χ , as a function of the intergalactic grain size: (a) silicate case and (b) graphite case. The solid and dotted curves are based on the upper bounds of the intergalactic extinction and the reddening against distant supernovae, respectively. The thick and thin curves are the cases of low and high star formation histories, respectively.

than graphite in the optical bands. For $100 \text{ \AA} \lesssim a \lesssim 0.1 \mu\text{m}$, the upper bound of χ shows a local minimum corresponding to the peak shown in Figure 4. Finally, there is not any constraint of χ for a very large ($a \gtrsim 1 \mu\text{m}$) grain.

4 CONSTRAINT FROM IGM THERMAL HISTORY

As shown in the previous paper (Inoue & Kamaya 2003), we show the amount of the IG dust is constrained by using the thermal history of the IGM. When a dust grain is hit by a photon with an energy larger than a critical value, an electron escapes from the grain; photoelectric effect. Such a photoelectron contributes to the gas heating if its energy is larger than the mean kinetic energy of gas particles. As shown in Appendix A (see also Nath, Sethi, & Shchekinov 1999; Inoue & Kamaya 2003), the photoelectric heating by dust grains is comparable with, and sometimes dominate, the atomic photoionization heating in the IGM. Of course, the efficiency of the dust heating depends on the dust amount. If a model of the IGM has too much dust, the theoretical temperature of IGM exceeds the observational one owing to the dust photoelectric heating. Therefore, we can put an upper bound of the amount of the IG dust so as to keep the consistency between the theoretical IGM temperature and the observed one. In the next subsection, we describe how to calculate the thermal history of IGM affected by the dust photoelectric heating. An upper bound of χ , which represents the amount of the IG dust, is estimated in subsection 4.2.

4.1 Thermal history of IGM

In this paper, we consider only a mean temperature of the IGM, T_{IGM} , for simplicity. The T_{IGM} time-evolution is described by (e.g., Hui & Gnedin 1997)

$$\frac{dT_{\text{IGM}}}{dt} = -2HT_{\text{IGM}} - \frac{T_{\text{IGM}}}{X} \frac{dX}{dt} + \frac{2(\Gamma - \Lambda)}{3k_{\text{B}}Xn_{\text{b}}}, \quad (6)$$

where H is the Hubble constant, n_{b} is the cosmic mean number density of baryon, Γ and Λ are the total heating and cooling rates per unit volume, respectively, X is the number ratio of the total gaseous particles to the baryon particles, i.e., $X \equiv \sum n_i/n_{\text{b}}$, where n_i is the number density of the i -th gaseous species and we consider H I, H II, He I, He II, He III, and electron. We neglect the effect of helium and metal production by stars on the chemical abundance for simplicity. Fortunately, their time variation in mass is not significant relatively to the total mass. Indeed, the metal mass fraction reaches at the most 0.002 (Figure 2). The number ratio of helium to hydrogen is always about 0.1 after the Big-bang. A constant mass fraction ($Y = 0.24$) of helium is assumed throughout our calculation.

We solve equation (6) coupled with non-equilibrium rate equations for these gaseous species. These rate equations with rate coefficients and the heating/cooling rates are summarised in Appendix B. In the calculation, the time-step is adjusted to being 1/1000 of

the time-scale of the HI/HII transition. The number density of the IG dust at each redshift is determined by equation (1), (2), and (5) with a parameter of χ . The grain charge and heating/cooling rates are determined by a standard manner which is described in Appendix A.

The initial condition is as follows: the starting redshift is $z = 3.4$, at which it is considered that the HeII reionization occurred (e.g., Theuns et al. 2002a). The initial temperature is set to be 25,000 K, which is the mean IGM temperature at the redshift suggested by the Lyman α forest in QSO spectra (Schaye et al. 2000; Theuns et al. 2002b). We assume an ionization equilibrium balanced between the recombination and the photoionization as the initial chemical abundance. In each time step, the calculated chemical abundance at $z < 3.4$ reaches almost another ionization equilibrium balanced among the recombination, the photoionization, and the collisional ionization.²

The background radiation is required to calculate the IGM thermal history. We assume a power-law background radiation; its mean intensity at a frequency of ν is $J_\nu = J_L(\nu/\nu_L)^{-\alpha}$, where J_L and ν_L are the mean intensity and the frequency at the hydrogen Lyman limit. We also assume that the spectral index, α , is constant but the intensity, J_L , evolves along the redshift. In Figure 6, such an evolution is displayed. The data are taken from Scott et al. (2002) who investigate the QSO proximity effect on the number density of the Lyman α forest in spectra of QSOs at $z = 0-5$, and estimate the Lyman limit intensity of the background radiation in the redshift range. Here, we use a fitting formula as

$$\frac{J_L}{\text{erg s}^{-1} \text{cm}^{-2} \text{sr}^{-1} \text{Hz}^{-1}} \approx 2.5 \times 10^{-23} (1+z)^{2.5} \quad (7)$$

for $0 \lesssim z \lesssim 4$, which is shown in Figure 6 as the solid line. The background radiation at $z \lesssim 3$ is likely to be dominated by QSOs. Hence, we consider two cases of $\alpha = 1$ and 2. Such values of α are consistent with the QSO dominated background radiation (Haardt & Madau 1996; Zheng et al. 1997).

In Figure 7, we show some examples of the IGM thermal history, assuming $0.1 \mu\text{m}$ IG dust and the spectral index of $\alpha = 1$. In each panel, six cases of χ are depicted as the solid curves. By definition of χ (eq.[3]), $\chi = 1$ means that all metal in the universe is condensed into the IG dust, and $\chi = 0$ means no IG dust. The observational data are taken from Schaye et al. (2000). They observe the Ly α clouds with the column density of 10^{13-15}

² Since the collisional ionization plays only a minor role, the calculated chemical abundance is different slightly from the abundance in the recombination-photoionization equilibrium.

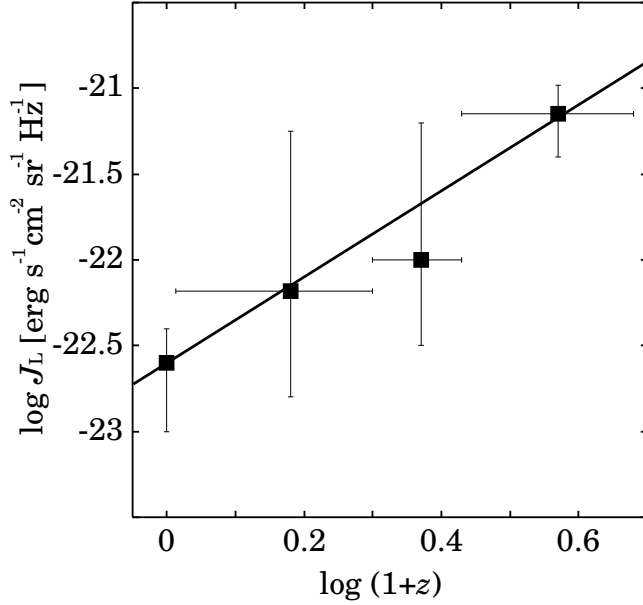


Figure 6. Redshift evolution of ionizing background intensity. Data points with error-bars are taken from Scott et al. (2002). The solid line is an analytical fit described in equation (8).

cm⁻² (i.e., slightly over density regions), and convert the temperature of the clouds into that at the mean density of the IGM by using the equation of state of the IGM. Thus, we can compare both thermal histories directly. In the next subsection, such a comparison is presented quantitatively.

4.2 Constraint for χ from thermal history of IGM

Once theoretical histories of IGM temperature are obtained, the amount of IG dust is constrained from the comparison of the theoretical temperature with observational one. Hence, we compare our theoretical thermal histories with 10 observational points at the range of $1.5 < z < 3.4$ of Schaye et al. (2000). We reject a case of too much χ by the least squares method. The rejection criterion is the significance level less than 30% in χ^2 -test. The obtained upper bound of χ is shown in Figure 8 as a function of the grain size. In this figure, the solid curves are the upper bound obtained from the thermal history. The results of figure 5 are overlaid as the dotted and dashed curves. The thick and thin curves are the cases of low and high star formation histories, respectively. Each panel shows the results: (a) silicate and spectral index of background radiation of $\alpha = 1$, (b) graphite and $\alpha = 1$, (c) silicate and $\alpha = 2$, and (d) graphite and $\alpha = 2$, respectively.

Combining constraints from the thermal history with those from distant SNe, we obtain the rejected range of χ as a function of the IG grain size, which is depicted as the thick and

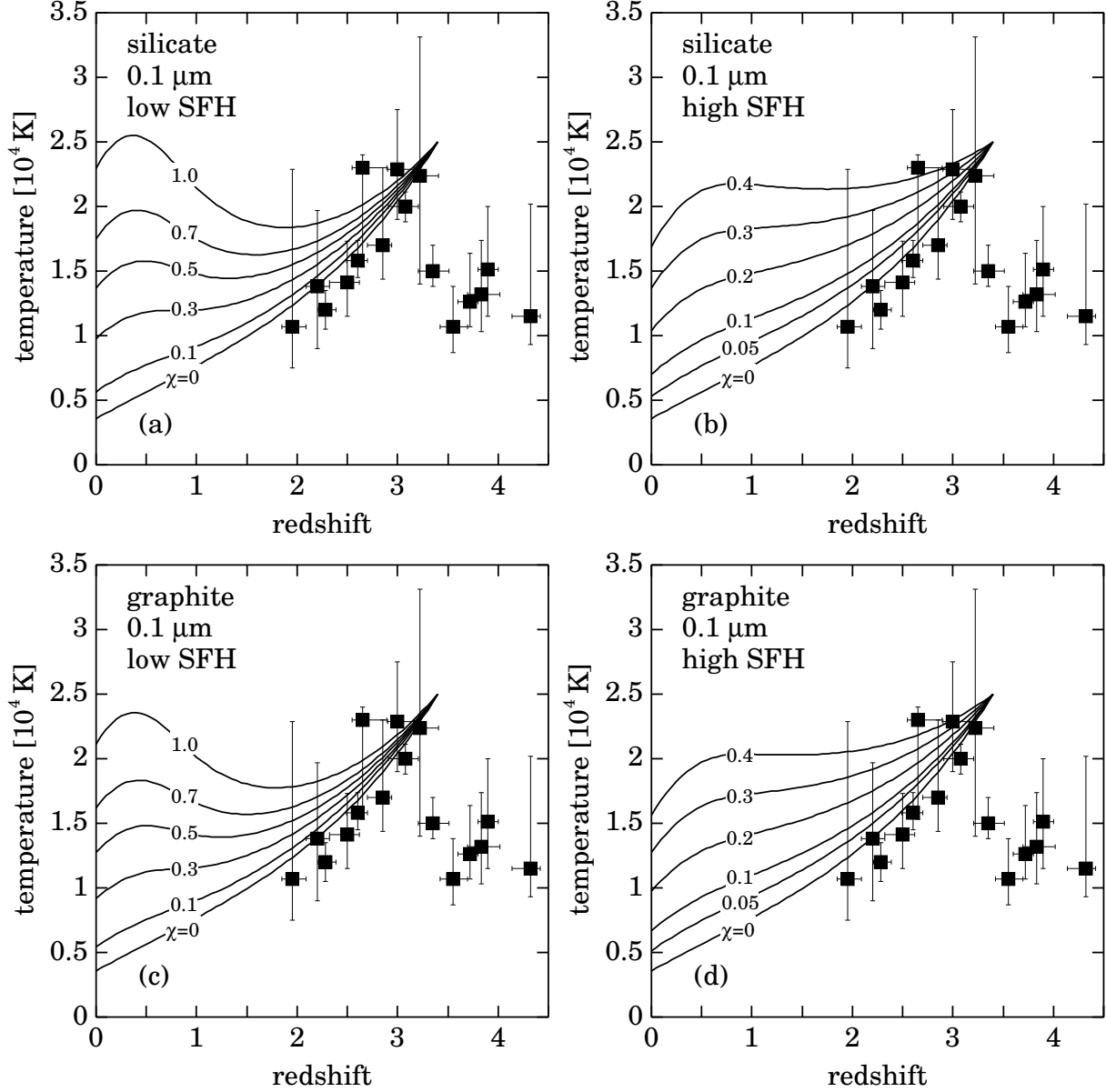


Figure 7. Examples of the IGM thermal history: (a) silicate and low star formation history (SFH), (b) silicate and high SFH, (c) graphite and low SFH, and (d) graphite and high SFH. The assumed grain size is $0.1 \mu\text{m}$. Six solid curves in each panel are the thermal histories assumed the value of χ , the mass ratio of the IG dust to the total metal, indicated on each curve. The data points are taken from Schaye et al. (2000). The spectral index of the background radiation is assumed to be unity.

thin shaded areas in Figure 8. The combined upper bounds of χ is also summarised in Table 1. We find a rough upper bound of χ as 0.1 with a factor of a few uncertainty, except for a very large ($\sim 1 \mu\text{m}$) case and a medium-size ($\sim 100 \text{ \AA}$) silicate of $\alpha = 2$.

The upper bound of χ from the thermal history has a positive dependence of grain size. This corresponds to the fact that the dust heating rate has a negative dependence of grain size (see Figure A3). Especially, for small silicate grain, we obtain a strict upper bound of χ from the thermal history, whereas observations of distant SNe cannot provide any constraints.

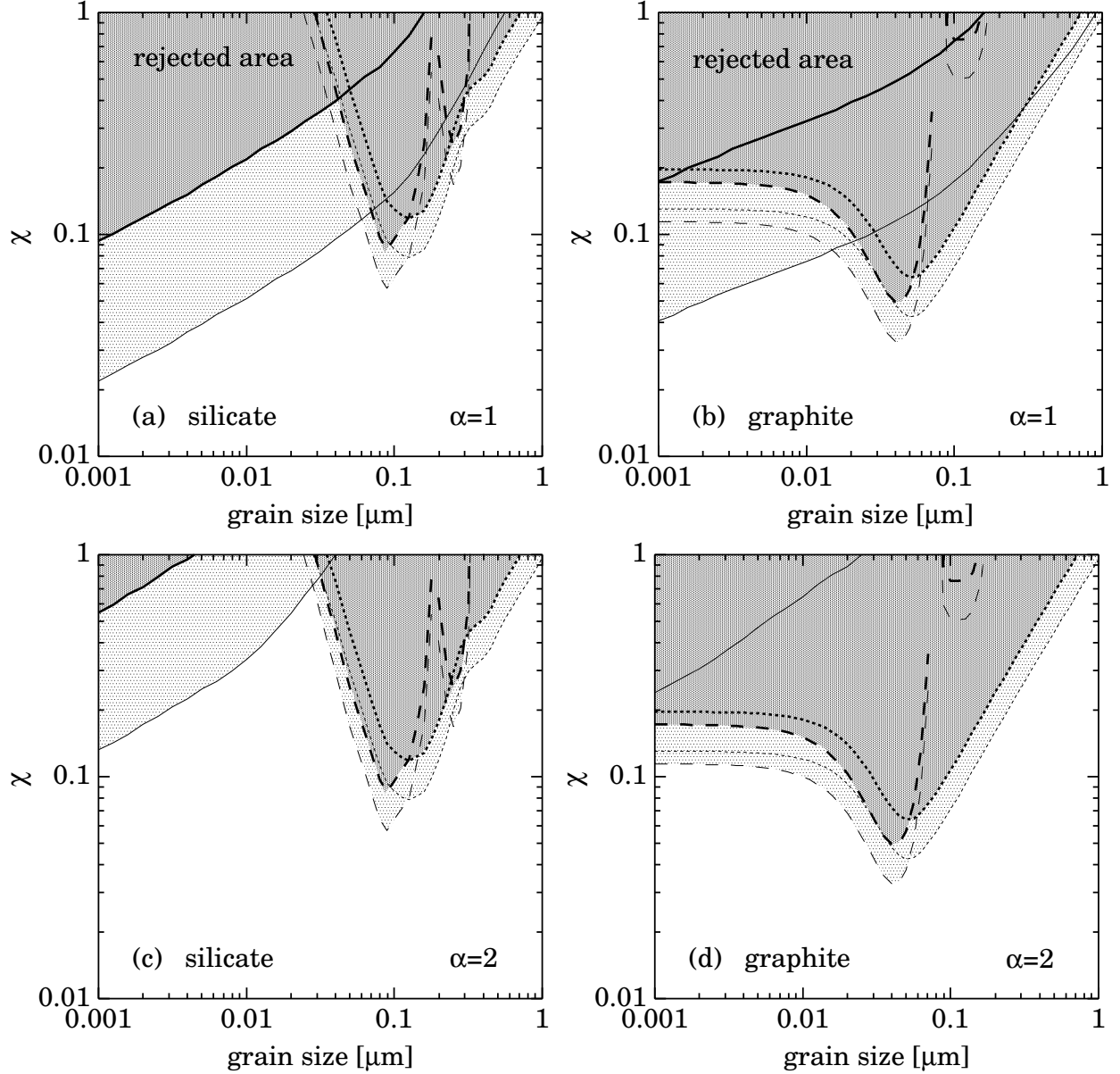


Figure 8. Rejected area of χ , the mass ratio of the IG dust to the total metal as a function of the IG grain size: (a) silicate and spectral index of background radiation $\alpha = 1$, (b) graphite and $\alpha = 1$, (c) silicate and $\alpha = 2$, and (d) graphite and $\alpha = 2$. The solid curves are the upper bound obtained from the thermal history. The dotted and dashed curves are the upper bounds from observations of distant SNe (Figure 5). The thick and thin curves are the cases of low and high star formation histories, respectively. In panel (d), there is no constraint from the thermal history of the low SFH case.

We comment that the upper bound of χ for small silicate is smaller than that for small graphite. This is why a small ($a \lesssim 0.1\mu\text{m}$) silicate has a larger efficiency factor for absorption than that of graphite in the UV–X-ray regime. Hence the grain potential, mean photoelectron energy, and heating rate of small silicate are larger than those of graphite (Figures A1–A3). Moreover, we find a positive dependence of the spectral index α against the obtained upper bounds of χ , which is due to the negative dependence of α against the dust heating rate (Figure A3).

Table 1. Upper bounds of χ

silicate				
$\alpha = 1$	low SFH		high SFH	
10 Å	0.093	TH ^a	0.022	TH
100 Å	0.22	TH	0.051	TH
0.1 μm	0.096	SNe ^b	0.064	SNe
1 μm	1.0	def ^c	0.97	SNe
$\alpha = 2$	low SFH		high SFH	
10 Å	0.55	TH	0.13	TH
100 Å	1.0	def	0.34	TH
0.1 μm	0.096	SNe	0.064	SNe
1 μm	1.0	def	0.97	SNe
graphite				
$\alpha = 1$	low SFH		high SFH	
10 Å	0.17	SNe	0.041	TH
100 Å	0.15	SNe	0.076	TH
0.1 μm	0.11	SNe	0.071	SNe
1 μm	1.0	def	0.95	SNe
$\alpha = 2$	low SFH		high SFH	
10 Å	0.17	SNe	0.11	SNe
100 Å	0.15	SNe	0.10	SNe
0.1 μm	0.11	SNe	0.071	SNe
1 μm	1.0	def	0.95	SNe

^a By thermal history.^b By SNe observations^c By definition

5 DISCUSSION

We have obtained upper bound of χ as a function of grain size from observations of distant SNe and comparison of theoretical IGM thermal history with observational one. Here we discuss what our results imply.

5.1 Allowable amount of IG dust

How much dust can exist in the IGM? Once assuming a value of χ , we obtain the IG dust density via equation (5). In Figure 9, we show the upper bounds of the IG dust mass density and \mathcal{D}^{IGM} as a function of redshift. The solid and dashed curves are the cases of low and high SFHs, respectively. The assumed upper bound of χ is 0.1 for both cases of SFHs. The uncertainty of this value of χ is about a factor of a few as long as the IG grain size is smaller than 1 μm and the background spectral index $\alpha = 1$ (see also Figure 8 and Table 1). We find that the upper bound of the local ($z \sim 0$) universe is determined well; the local IG dust density is less than about 10^{-34} g cm⁻³, or equivalently the dust-to-gas ratio is less than about 3×10^{-4} which is about 1/20 of the Galactic value. Along the redshift, the allowed dust density increases and the dust-to-gas ratio decreases. The increasing/decreasing rates change at $z \sim 1$ at which the $(1+z)$ dependence of the assumed SFH changes (eq.[1]). Taking

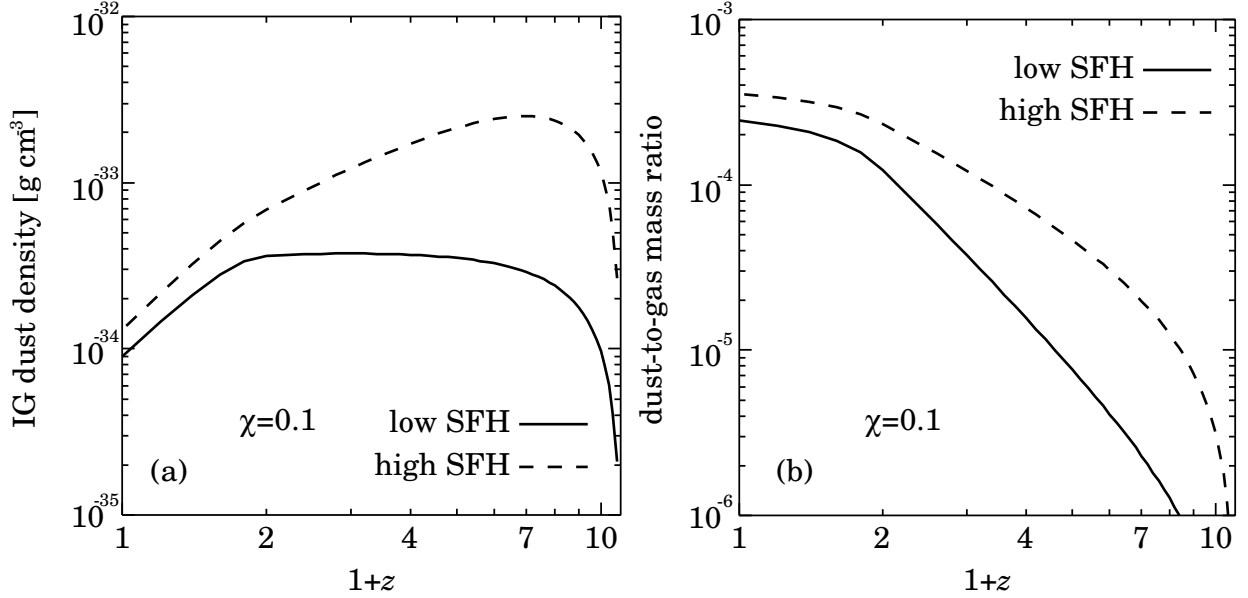


Figure 9. Maximum (a) IG dust density and (b) dust-to-gas mass ratio in the IGM as a function of redshift. In each panel, the solid and dashed curves are the cases of low and high star formation histories, respectively. The assumed χ , the mass ratio of the IG dust to the total metal in the universe, is 0.1.

into account a factor of 2 uncertainty of the upper bound of χ , we obtain the maximum IG dust density as

$$\frac{\rho_{\text{d,max}}^{\text{IGM}}(z)}{\text{g cm}^{-3}} = (2 - 8) \times 10^{-34} \begin{cases} \left(\frac{1+z}{2}\right)^{2.3} & (\text{for } z \leq 1) \\ \left(\frac{1+z}{2}\right)^{0-1.5} & (\text{for } z > 1) \end{cases}, \quad (8)$$

or the maximum dust-to-gas mass ratio as

$$\mathcal{D}_{\text{max}}^{\text{IGM}}(z) = (1 - 4) \times 10^{-4} \begin{cases} \left(\frac{1+z}{2}\right)^{-0.7} & (\text{for } z \leq 1) \\ \left(\frac{1+z}{2}\right)^{-(1.5-3)} & (\text{for } z > 1) \end{cases}. \quad (9)$$

The dust-to-gas ratio at $z \sim 3$ is consistent with the previous result by Inoue & Kamaya (2003).

5.2 IG extinction and reddening

In Figure 10, we show the upper bounds of IG extinction and reddening expected from the upper bounds of χ summarised in Table 1. Four cases of grain size as 10 Å, 100 Å, 0.1 μm, and 1 μm are indicated by blue, green, red, and cyan curves, respectively. Solid and dashed curves are the cases of low and high SFHs, respectively. And, thick and thin curves are the cases of the spectral index $\alpha = 1$ and 2, respectively. For grains of 0.1 μm and 1 μm, the upper bounds of χ are determined from SNe observations or the definition of χ (i.e. $\chi \leq 1$) as shown in Table 1. That is, these upper bounds of χ do not depend on the assumed background spectrum. Hence, the thick and thin curves of these cases are

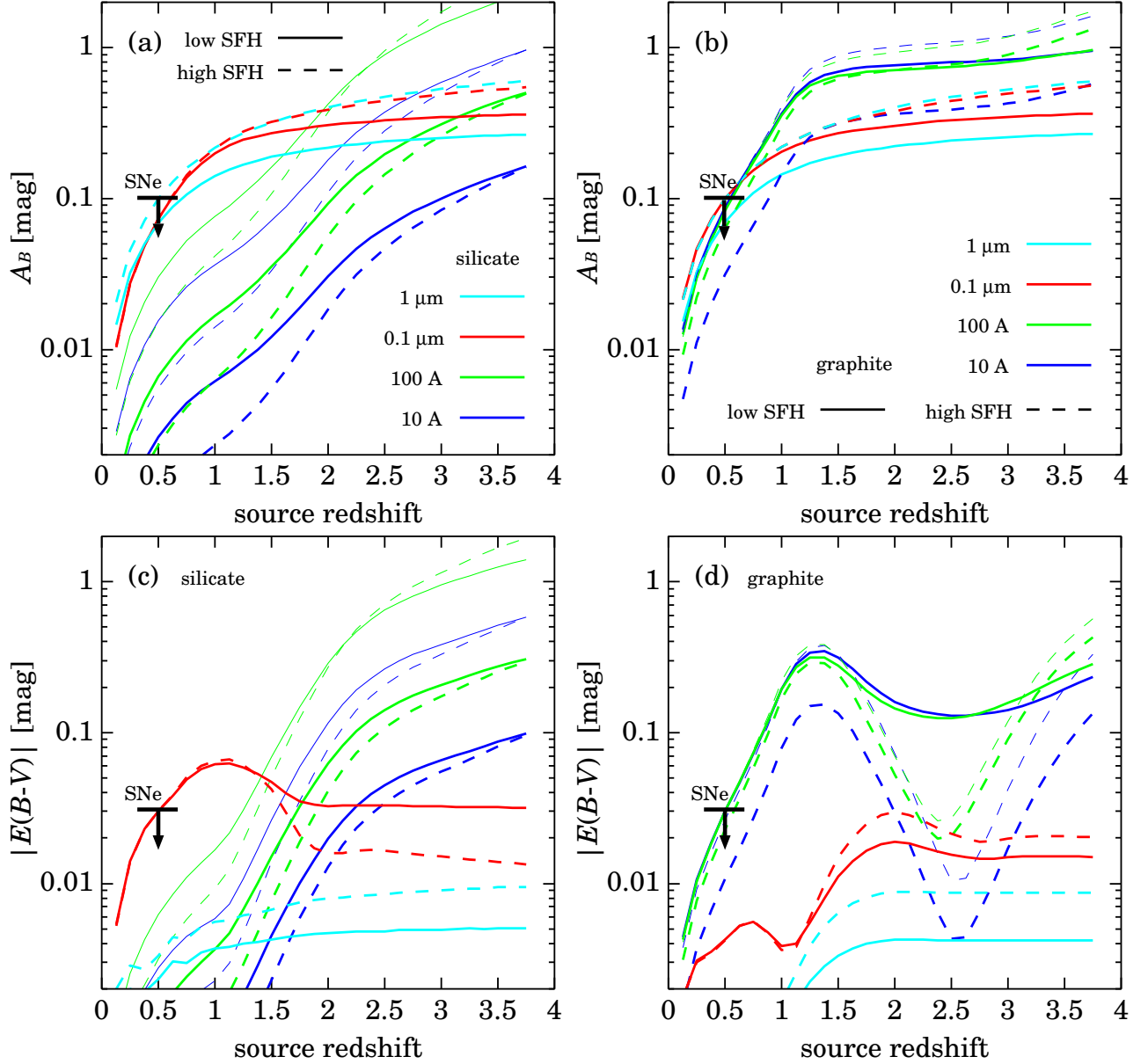


Figure 10. Maximum intergalactic extinction and reddening against a source at a redshift; observer’s B -band extinction of (a) silicate case and (b) graphite case, and colour excesses between B and V -bands in observer’s rest frame of (c) silicate case and (d) graphite case. Assumed χ values are summarised in Table 1. For blue, green, red, and cyan curves, we assumed the grain size of 10 Å, 100 Å, 0.1 μm, and 1 μm, respectively. Solid and dashed curves indicate the low and high star formation histories, respectively, and thick and thin curves indicate the background spectral indices of 1 and 2, respectively. The upper bounds from observations of distant SNe are shown as the downward arrows in each panel. The vertical axes of panels (c) and (d) are the absolute value of the colour excesses. Actually, colour excesses of 1 μm for silicate and of 0.1 μm and 1 μm for graphite are negative.

completely superposed on each other. The constraints from SNe observations of $A_B \leq 0.1$ mag and $|E(B - V)| \leq 0.03$ mag at $z = 0.5$ are also shown as the downward arrows in each panel. We note that the vertical axes of panels (c) and (d) are the absolute value of colour excess. Indeed, colour excesses of 1 μm for silicate, and of 0.1 μm and 1 μm for graphite are negative.

We find that the upper bound of the IG extinction is ~ 0.2 mag for a source at $z = 1$

from panels (a) and (b) of Figure 10. This value agrees well with the result from SDSS quasars data by Mörtzell & Goobar (2003). For $z \gtrsim 1$ objects, the upper bound of the IG extinction becomes ~ 0.5 mag, and as an extreme case, we cannot reject the possibility of 1 mag IG extinction for a source at $z \sim 3$.

Interestingly, we can investigate the nature of the IG dust by using the IG reddening. For $z \gtrsim 1$ sources, the expected absolute value of colour excess by the IG grain larger than $\sim 0.1 \mu\text{m}$ is very small, at the most ~ 0.05 mag, whereas that by a smaller grain can reach 0.1 mag or more. Thus, it may be possible to determine a typical size of the IG grain from observations of colour excess against a source at $z \gtrsim 1$; the detection of $\gtrsim 0.1$ mag colour excess for such a source proves the existence of small ($\lesssim 100 \text{ \AA}$) IG grains. If the IG dust is dominated by such small grains, the composition of the IG dust can be found. The small graphite grains show a prominent absorption feature at 2175 \AA (see Figure 3). Thus, we expect a local minimum of colour excess for a source at $z \simeq 2.5$ as shown in panel (d) of Figure 10. Therefore, if we detect such a change of colour excess along the redshift, we can conclude that many small graphite grains exist in the IGM.

Observations to detect the IG extinction and reddening are very challenging but strongly encouraging. The high- z gamma-ray bursts can be good background light sources for such observations (Perna & Aguirre 2000).

5.3 Ejection efficiency of dust from galaxies

The dust-to-metal ratio in the Galaxy, δ_{MW} , is 0.3–0.5 (e.g., Spitzer 1978; Whittet 2003). We may consider the dust-to-metal ratio in the IGM, δ_{IGM} is equal to δ_{MW} , if δ_{MW} is typical for all galaxies, and metal and dust are ejected together from galaxies to the IGM keeping δ_{MW} . Is this thought compatible with the obtained upper bound of $\chi \lesssim 0.1$?

A fraction of metal produced by stars in galaxies exists out of galaxies. This escape fraction is defined as f_{esc} . While f_{esc} is still uncertain, an estimate of it is 50–75% (Aguirre 1999, and references therein). We shall define another parameter of the IGM metallicity; Z_{IGM} . Because of $\chi = \mathcal{D}^{\text{IGM}}/Z$ and $f_{\text{esc}} = Z_{\text{IGM}}/Z$, where Z is the total cosmic metallicity, we find $\delta_{\text{IGM}} = \mathcal{D}^{\text{IGM}}/Z_{\text{IGM}} = \chi/f_{\text{esc}}$. Unless f_{esc} is less than ~ 0.5 , δ_{IGM} is estimated to be smaller than 0.2. Therefore, our result of $\chi \lesssim 0.1$ with $f_{\text{esc}} \sim 0.5$ may indicate that $\delta_{\text{IGM}} < \delta_{\text{MW}}$.

If that is true, we have to consider some mechanisms to reduce δ_{IGM} during the dust

transfer. For example, dust destruction during the transfer from galaxies to the IGM (Aguirre 1999), and/or different ejection efficiencies between metal and dust. Time evolution of the dust-to-metal ratio in galaxies may be also important. As shown by Inoue (2003), the dust-to-metal ratio in younger galaxies (i.e., higher- z galaxies) may be much smaller ($\sim 70\%$ off) than the present value of the Galaxy. In the case, a time-averaged δ_{MW} can become smaller than the current δ_{MW} adopted above, so that our constraint of χ may be cleared. In any case, we cannot obtain a rigid quantitative conclusion at the moment, because uncertainties are still very large. Further studies of this issue are very interesting.

5.4 IGM temperature at low redshift

As shown in Nath et al. (1999) and Appendix A, the dust photoelectric heating becomes more efficient for a lower gas density. Although the background intensity decreases along the redshift (Figure 6), the decrement of gas density is more efficient than the decrement of the background intensity, so that the importance of the dust heating increases for a lower redshift. While we obtained constraints of the amount of the IG dust from the IGM temperature at $z \simeq 2\text{--}3$ in section 4, the IGM temperature at a lower redshift of $z \lesssim 1$ provides us with a further constraint of the IG dust. Therefore, to measure the IGM temperature at $z \lesssim 1$ is very interesting.

Here, we show how much temperature is allowed by our upper bounds of χ . Figure 11 shows the IGM thermal histories assumed the upper bounds of χ in Table 1. The temperatures shown in the figure are upper bounds, which is denoted as $T_{\text{IGM,up}}$. In each panel, 18 thermal histories are shown; no IG dust with $\alpha = 1$ and 2 cases (thick and thin black solid curves), and 10 Å (blue), 100 Å (green), 0.1 μm (red), and 1 μm (cyan) IG dust with low (solid) or high (dash) SFHs and $\alpha = 1$ (thick) or 2 (thin) cases.

We find that for a smaller ($\lesssim 100$ Å) grain case, except for graphite of $\alpha = 2$, $T_{\text{IGM,up}}$ at $z \lesssim 1$ is still much higher than 10,000 K. On the other hand, for a larger ($\gtrsim 0.1$ μm) case, except for 1 μm graphite with high SFH and $\alpha = 1$, $T_{\text{IGM,up}}$ at $z \lesssim 1$ becomes lower than 10,000 K as well as no IG dust case. Therefore, we may conclude that IG grains are small if temperature higher than 10,000 K is observed at $z \lesssim 1$. Conversely, a lower IGM temperature at $z \lesssim 1$ provides us with a very strict constraint against small IG dust.

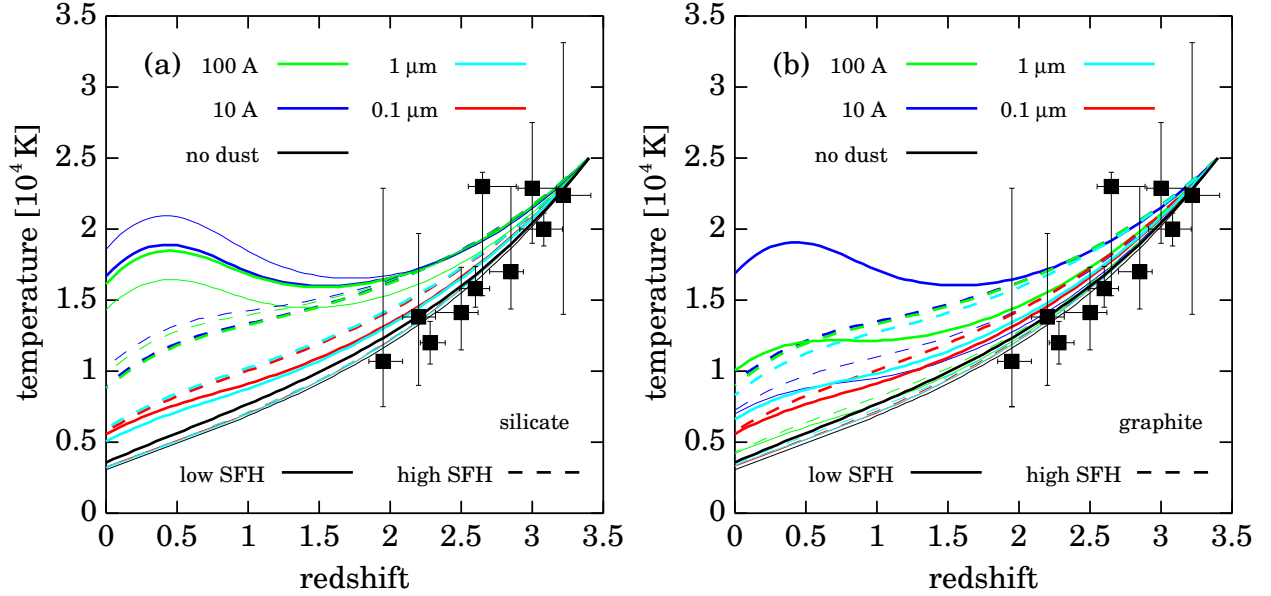


Figure 11. Maximum IGM temperatures corresponding to the upper bounds of χ in Table 1; (a) silicate case, (b) graphite case. Blue, green, red, and cyan curves are the cases of grain size of 10 Å, 100 Å, 0.1 μm, and 1 μm, respectively, and black curves are no IG dust cases. Solid and dashed curves indicate the low and high star formation histories, respectively, and thick and thin curves indicate the background spectral indices of 1 and 2, respectively. The data points are taken from Schaye et al. (2000).

6 CONCLUSION

We investigate the amount of the IG dust allowed by current observations of distant SNe and temperature of the IGM. The allowed amount of the IG dust is described as the upper bound of χ , the mass ratio of the IG dust to the total metal in the Universe. To specify χ , two models of cosmic history of metal production rate are assumed. That is, we assume two cosmic star formation histories expected from the recent observation of the high redshift objects. Our conclusions are as follows:

(1) Combining constraints from the IGM thermal history with those from distant SNe observations, we obtain the upper bounds of χ as a function of grain size in the IGM; roughly $\chi \lesssim 0.1$ for $10 \text{ Å} \lesssim a \lesssim 0.1 \text{ μm}$, and $\chi \lesssim 0.1(a/0.1 \text{ μm})^{-1}$ for $0.1 \text{ μm} \lesssim a \lesssim 1 \text{ μm}$.

(2) The upper bound of $\chi \sim 0.1$ corresponds to the upper bound of the IG dust density; the density increases from $\sim 10^{-34} \text{ g cm}^{-3}$ at $z = 0$ to $\sim 10^{-33} \text{ g cm}^{-3}$ at $z \sim 1$, and keeps a constant value or slowly increases toward higher redshift.

(3) The expected IG extinction against a source at $z \sim 1$ is less than $\sim 0.2 \text{ mag}$ at the observer's B -band. For higher redshift sources, we cannot reject the possibility of 1 mag extinction by the IG dust at the observer's B -band.

(4) Observations of colour excess against a source at $z \gtrsim 1$ provides us with information useful to constrain the nature of the IG dust. If we detect $\sim 0.1 \text{ mag}$ colour excess between

the observer's B and V -bands, a typical size of the IG dust is $\lesssim 100$ Å. Moreover, if there are many graphite grains of $a \lesssim 100$ Å in the IGM, we find a local minimum of the colour excess of a source at $z \sim 2.5$ corresponding to 2175 Å absorption feature.

(5) If half of metal produced in galaxies exists in the IGM, the obtained upper bound of $\chi \sim 0.1$ means that the dust-to-metal ratio in the IGM is smaller than the current Galactic value. It suggests that some mechanisms to reduce the dust-to-metal ratio in the IGM are required. For example, dust destruction in transfer from galaxies to the IGM, selective transport of metal from galaxies, and time evolution of the dust-to-metal ratio in galaxies (i.e., a smaller value for younger galaxies).

(6) Although we obtain constraints of the IG dust from the IGM temperature at $z \sim 2-3$, the temperature at $z \lesssim 1$ provides us with a more strict constraint of the IG dust. For example, the detection of temperature higher than 10,000 K at $z \lesssim 1$ suggests that the IG dust is dominated by small ($\lesssim 100$ Å) grains.

ACKNOWLEDGMENTS

We have appreciated informative comments presented by Prof. B. Draine, and discussions with Prof. A. Ferrara, Dr. S. Bianchi, and Dr. H. Hirashita. We are also grateful to Profs. T. Nakamura, S. Mineshige, and I.-S. Inutsuka for their encouragement. This work is supported by a Grant-in-Aid for the 21st Century COE "Center for Diversity and Universality in Physics". AKI is supported by the Research Fellowships of the Japan Society for the Promotion of Science for Young Scientists.

REFERENCES

- Aguirre, A., 1999, ApJ, 525, 583
- Aguirre, A., & Haiman, Z., 2000, ApJ, 532, 28
- Aguirre, A., Hernquist, L., Katz, N., Gardner, J., & Weinberg, D., 2001, ApJ, 556, L11
- Barger, A. J., Cowie, L. L., & Richards, E. A., 2000, AJ, 119, 2092
- Bouwens, R. J., et al., 2003, ApJ, in press (astro-ph/0306215)
- Bromm, V., Yoshida, N., & Hernquist, L. 2003, ApJ, 596, L135
- Buat, V., Boselli, A., Gavazzi, G., & Bonfanti, C., 2002, A&A, 383, 801
- Burstein, D., & Heiles, C., 1982, AJ, 87, 1165
- Calzetti, D., 2001, PASP, 113, 1449

- Cen, R., 1992, *ApJS*, 78, 341
- Cheng, F. H., Gaskell, C. M., & Koratkar, A. P., 1991, *ApJ*, 370, 487
- Connolly, A. J., Szalay, A. S., Dickinson, M., Subbarao, M. U., & Brunner, R. J., 1997, *ApJ*, 486, L11
- Cowie L. L, Songaila A., Kim T. S., & Hu E. M., 1995, *AJ*, 109, 1522
- Draine, B. T., 1978, *ApJS*, 36, 595
- Draine, B. T., & Lee, H. M., 1984, *ApJ*, 285, 89
- Draine, B. T., & Hao, L., 2002, *ApJ*, 569, 780
- Dunne, L., Eales, S., Ivison, R., Morgan, H., & Edmunds, M. 2003, *Nature*, 424, 285
- Elfgren, E., & Désert, F.-X. 2003, *A&A*, submitted (astro-ph/0310135)
- Ferrara, A., Aiello, S., Ferrini, F., & Barsella, B., 1990, *A&A*, 240, 259
- Ferrara, A., Ferrini, F., Barsella, B., & Franco, J., 1991, *ApJ*, 381, 137
- Ferrara, A., Nath, B., Sethi, S. K., & Shchekinov, Y., 1999, *MNRAS*, 303, 301
- Gallego, J., Zamorano, J., Aragon-Salamanca, A., & Rego, M., 1995, *ApJ*, 455, L1
- Giavalisco, M., et al. 2003, *ApJL*, in press (astro-ph/0309065)
- Goobar, A., Bergstöm, L., & Mörtzell, E., 2002, *A&A*, 384, 1
- Haardt, F., & Madau, P., 1996, *ApJ*, 461, 20
- Hui, L., & Gnedin, N. Y., 1997, *MNRAS*, 292, 27
- Inoue, A. K., 2003, *PASJ*, 55, in press (astro-ph/0308204)
- Inoue, A. K., & Kamaya, H., 2003, *MNRAS*, 341, L7
- Iwata, I., Ohta, K., Tamura, N., Ando, M., Wada, S., Watanabe, C., Akiyama, M., & Aoki, K., 2003, *PASJ*, 55, 415
- Jaffe, A. H., et al., 2001, *Phys.Rev.Lett.*, 86, 3475
- Kozasa, T., & Hasegawa, H. 1987, *Prog. Theor. Phys.*, 77, 1402
- Laor, A., & Draine, B. T., 1993, *ApJ*, 402, 441
- Lilly, S. J., Le Fevre, O., Hammer, F., & Crampton, D., 1996, *ApJ*, 461, L1
- Loeb, A., & Haiman, Z., 1997, *ApJ*, 490, 571
- Madau, P., Ferguson, H. C., Dickinson, M. E., Giavalisco, M., Steidel, C. C., & Fruchter, A., 1996, *MNRAS*, 283, 1388
- Madau, P., Pozzetti, L., & Dickinson, M., 1998, *ApJ*, 498, 106
- Morgan, H. L., Dunne, L., Eales, S., Ivison, R., & Edmunds, M. G. 2003, *ApJL*, in press (astro-ph/0309233)
- Mörtzell, E., & Goobar, A., 2003, astro-ph/0308046

- Nath, B. B., Sethi, S. K., & Shchekinov, Y., 1999, MNRAS, 303, 1
- Nozawa, T., Kozasa, T., Umeda, H., Maeda, K., & Nomoto, Ken'ichi 2003, ApJ, in press (astro-ph/0307108)
- Osterbrock, D. E. 1989, *Astrophysics of Gaseous Nebulae and Active Galactic Nuclei* (Mill Valley: University Science Books)
- Paerels, F., Petric, A., Telis, G., & Helfand, D. J., 2002, BAAS, 201, 97.03
- Percival, W. J., et al., 2001, MNRAS, 327, 1297
- Perlmutter, S., et al., 1999, ApJ, 517, 565
- Perna, R., & Aguirre, A. 2000, ApJ, 543, 56
- Pryke, C., et al., 2002, ApJ, 568, 46
- Riess, A. G., et al., 1998, AJ, 116, 1009
- Riess, A. G., et al., 2001, ApJ, 560, 49
- Rowan-Robinson, M., Negroponte, J., & Silk, J., 1979, Nature, 281, 635
- Schaye, J., Theuns, T., Rauch, M., Efstathiou, G., & Sargent, W. L. W., 2000, MNRAS, 318, 817
- Schlegel, D. J., Finkbeiner, D. P., & Davis, M., 1998, ApJ, 500, 525
- Schneider, R., Ferrara, A., & Salvaterra, R. 2003, MNRAS, submitted (astro-ph/0307087)
- Scott, J., Bechtold, J., Morita, M., Dobrzycki, A., & Kulkarni, V. P., 2002, ApJ, 571, 665
- Songaila, A. 2001, ApJ, 561, L153
- Spergel, D. et al., 2003, ApJ, in press (astro-ph/0302209)
- Spitzer, L., 1978, *Physical Processes in the Interstellar Medium*, Wiley, New York
- Steidel, C. C., Adelberger, K. L., Giavalisco, M., Dickinson, M., & Pettini, M., 1999, ApJ, 519, 1
- Sutherland, R. S., & Dopita, M. A., 1993, ApJS, 88, 253
- Takase, B. 1972, PASJ, 24, 295
- Telfer, R. C., Kriss, G. A., Zheng, W., Davidsen, A. F., & Tytler, D., 2002, ApJ, 579, 500
- Telis, G. A., Petric, A., Paerels, F., & Helfand, D. J., 2002, BAAS, 201, 79.12
- Theuns, T., et al., 1998, MNRAS, 301, 478
- Theuns, T., et al., 2002a, ApJ, 574, L111
- Theuns, T., et al., 2002b, ApJ, 567, L103
- Todini, P., & Ferrara, A., 2001, MNRAS, 325, 726
- Tresse, L., & Maddox, S. J., 1998, ApJ, 495, 691
- Weingartner, J. C., & Draine, B. T., 2001a, ApJ, 548, 296

Weingartner, J. C., & Draine, B. T., 2001b, *ApJS*, 134, 263

Whittet, D. C. B., 2003, *Dust in the Galactic Environment* 2nd edition (Bristol: Institute of Physics)

Windt, D. L. 2002, *ApJ*, 564, L61

Wright, E. L., 1981, *ApJ*, 250, 1

Zheng, W., Kriss, G. A., Telfer, R. C., Grimes, J. P., & Davidsen, A. F., 1997, *ApJ*, 475, 469

APPENDIX A: DUST PHOTOELECTRIC HEATING IN IGM

The dust photoelectric effect in the IGM is summarised. The basic equations are presented in various places, for example, section 2 in Inoue & Kamaya (2003). More detailed information of the issue can be found in Weingartner & Draine (2001b).

We consider spherical silicate and graphite grains. Under a condition suitable for the IGM (low density and intense UV radiation), these grains have a positive electric charge, which is determined by the competition between the collisional electron capture and the photoelectric ionization. The electron stripping by the colliding ions is negligible, while the proton collision is included in the calculation for making the following figures. The charge on grains is in an equilibrium state, which is achieved quickly (~ 10 – 100 yr).

The input parameters to obtain the equilibrium charge are grain type, grain size, gas density, gas temperature, radiation intensity, and radiation spectrum. We assume the incident radiation spectrum to be a power-law. In Figure A1, we show these dependences of the equilibrium grain potential energy normalized by the gas kinetic energy, i.e., $eU/k_{\text{B}}T = Z_{\text{d}}e^2/ak_{\text{B}}T$, where U is the grain potential, Z_{d} is the grain charge, a is the grain size, T is the gas temperature, e is the electron charge, and k_{B} is the Boltzmann constant. We examine three cases of the power-law index of the incident radiation, $\alpha = 1, 2$, and 5 , where the mean intensity is J_{ν} and proportional to $\nu^{-\alpha}$. While the spectrum of the incident radiation is rather uncertain, it is likely to be a power-law with index of 1–2 if the radiation is dominated by QSOs (e.g., Haardt & Madau 1996; Zheng et al. 1997). The case of $\alpha = 5$ corresponds to the stellar radiation dominated case for a comparison. In each panel of Figure A1, a parameter set of nominal values is assumed except for the parameter of the horizontal axis, but it may be suitable for the IGM at $z \sim 3$. These values are indicated in the panels; $a_{-5} = a/0.1\mu\text{m}$,

$n_{,-5} = n/10^{-5} \text{ cm}^{-3}$, $T_4 = T/10^4 \text{ K}$, and $J_{,-21} = J_{\nu_L}/10^{-21} \text{ erg s}^{-1} \text{ cm}^{-2} \text{ sr}^{-1} \text{ Hz}^{-1}$, where ν_L is the Lyman limit frequency.

The dotted lines in Figure A1 (a) and (c) indicate an upper limit of the grain potential based on an estimate of the critical potential for the ion field emission (Draine & Hao 2002); $eU/k_B T \lesssim 3500(T/10^4 \text{ K})^{-1}(a/0.1 \mu\text{m})$. If the grain potential exceeds this upper limit, singly charged ions may escape one by one from the grain surface, so that the grain is destroyed gradually. For panels (b) and (d), this upper limit is out of the panels. We can conclude that this process is not so important for our interesting.

In Figure A2, we show a mean photoelectron energy from dust grains normalized by the gas kinetic energy, $\langle E_{\text{pe}} \rangle / k_B T$, as a function of (a) grain size, (b) gas density, (c) gas temperature, and (d) radiation intensity. Moreover, the ratio of the dust photoelectric heating rate to the hydrogen photoionization heating rate ($\Gamma_{\text{pe}}/\Gamma_{\text{Hpi}}$) is depicted as a function of these quantities in Figure A3. For the dust heating rate, we assume the dust-to-gas mass ratio to be 10^{-4} as a nominal value, which is about 1/100 of the Galactic dust-to-gas mass ratio.

The obtained results are roughly consistent with those of Nath, Sethi, & Shchekinov (1999). While some quantitative differences are seen between our results and theirs, they may be caused by differences of the adopted photoelectric yield, absorption efficiency factors, and radiation spectrum.

In summary, We find that the dust photoelectric heating exceeds the photoionization heating for a case of a smaller grain size, a lower gas density, a higher temperature, a more intense radiation, or a harder radiation spectrum. Furthermore, we find that silicate and graphite grains show similar results, and all of $eU/k_B T$, $\langle E_{\text{pe}} \rangle / k_B T$, and $\Gamma_{\text{pe}}/\Gamma_{\text{Hpi}}$ show a power-law like dependence of grain size, gas density, gas temperature, and radiation intensity.

A1 Analytic investigation

We investigate dependences found in Figures A1–A3 analytically with some approximations, here. However, all results concerning dust grains used in section 4 are calculated numerically.

Let us express $eU/k_B T$ as x . When the electron capture rate balances with the photoelectric ionization, we have

$$s_e n_e \langle v_e \rangle (1 + x) = \int Q_\nu Y_\nu \frac{4\pi J_\nu}{h\nu} d\nu, \quad (\text{A1})$$

where s_e is the sticking coefficient for an electron collision, n_e is the electron number density, $\langle v_e \rangle$ is the mean kinetic velocity of electron, Q_ν is the absorption efficiency factor of grains,

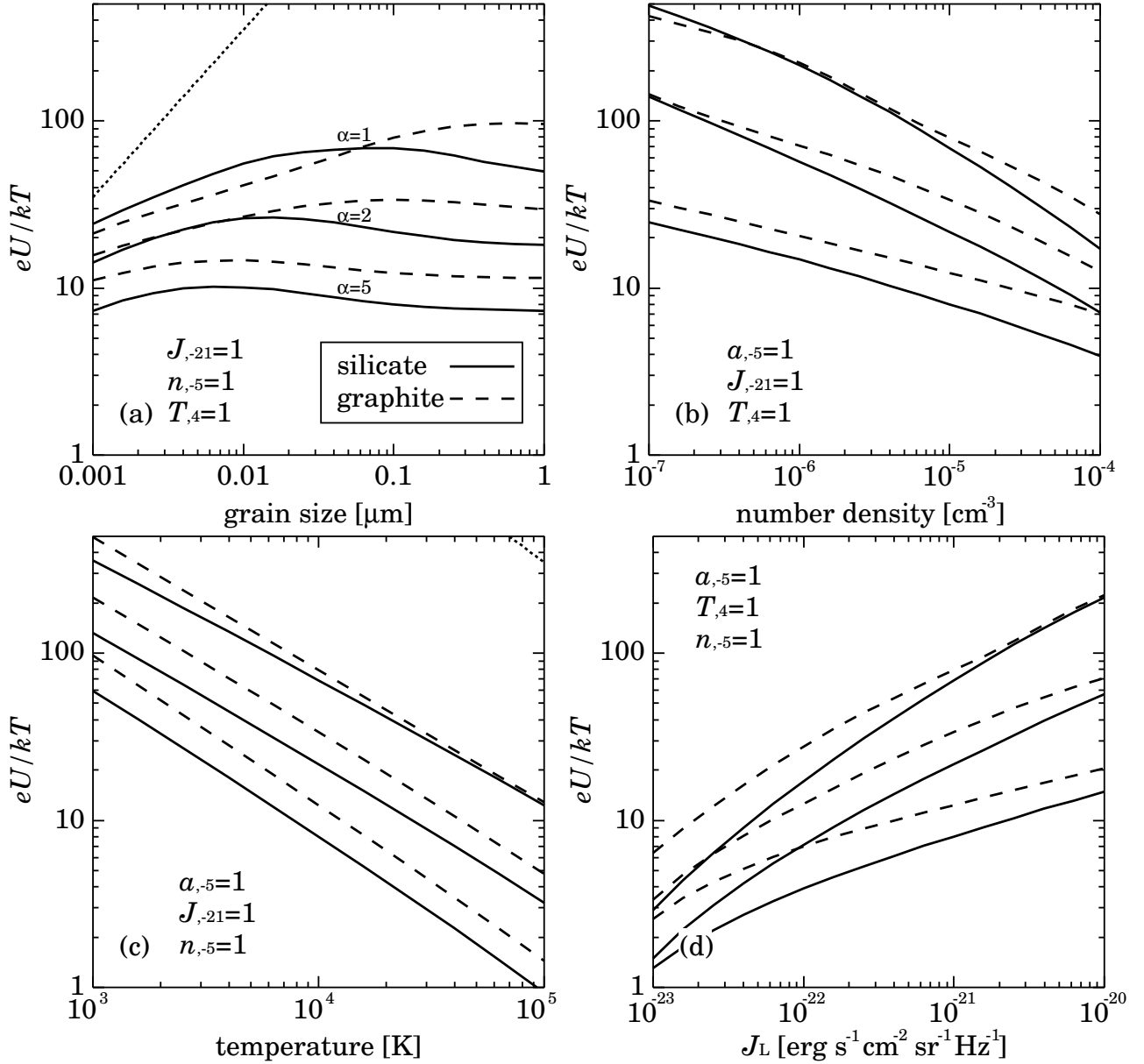


Figure A1. Normalized equilibrium potential of grains as a function of (a) grain size, (b) gas number density, (c) gas temperature, and (d) mean intensity at the Lyman limit. The solid and dashed curves indicate silicate and graphite cases, respectively. For the incident radiation, we consider three cases of the power-law index, $J_\nu \propto \nu^{-\alpha}$; $\alpha = 1, 2$, and 5 from top to bottom curves in each panel. Except for the parameter of the horizontal axis, a parameter set of nominal values is assumed. These values are indicated in each panel; $a_{,-5} = a/0.1 \mu\text{m}$, $n_{,-5} = n/10^{-5} \text{ cm}^{-3}$, $T_{,4} = T/10^4 \text{ K}$, and $J_{,-21} = J_\nu/10^{-21} \text{ erg s}^{-1} \text{ cm}^{-2} \text{ sr}^{-1} \text{ Hz}^{-1}$, where ν_L is the Lyman limit frequency. The dotted lines in panels (a) and (c) indicate an upper limit of the grain potential (Draine & Hao 2002).

Y_ν is the photoelectric yield, and J_ν is the mean intensity of the incident radiation. The left-hand side of the above equation is the electron capture rate per unit area, and the right-hand side is the photoelectric ionization rate per unit area.

The photoelectric yield can be given approximately by (Draine 1978)

$$Y_\nu \approx Y_\infty \left(1 - \frac{I_p}{h\nu} \right) \quad (\text{A2})$$

for $h\nu > I_p$ and $Y_\nu \approx 0$ for otherwise, where I_p is the ionization potential and $I_p \simeq W +$

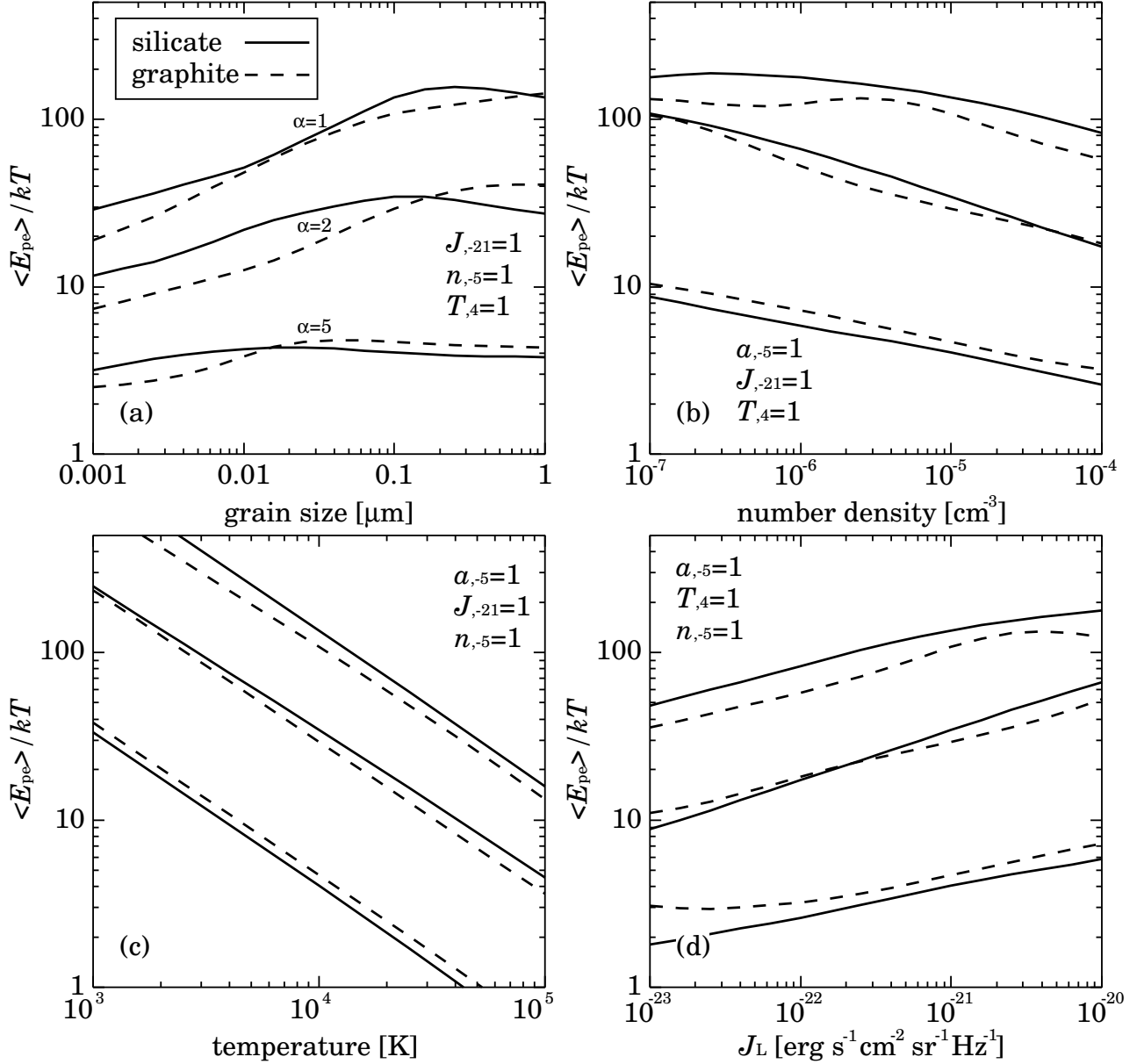


Figure A2. Mean energy of dust photoelectron normalized by gas kinetic energy as a function of (a) grain size, (b) gas number density, (c) gas temperature, and (d) mean intensity at the Lyman limit. Notations are the same as Figure A1.

$xk_B T$ with W being the work function. We adopt a power-law spectrum for the radiation, $J_\nu = J_L(\nu/\nu_L)^{-\alpha}$, and an approximation form of the absorption efficiency factor as $Q_\nu \approx Q_L(\nu/\nu_L)^{-\beta}$, where ν_L is the Lyman limit frequency of hydrogen. For a grain larger than $\sim 0.1 \mu\text{m}$, $\beta \simeq 0$, and for a smaller grain, $\beta \simeq 1-2$. If we define a function as $f(h\nu) = QYJ/h\nu$, $\partial f/\partial h\nu = 0$ only when $h\nu = h\nu_* = I_p(\alpha+\beta+2)/(\alpha+\beta+1)$. Because the function of f has the peak at $h\nu_*$, the integral in equation (A1) is approximated to be $(4\pi/h)Q(h\nu_*)Y(h\nu_*)J(h\nu_*)$. If $x \gg 1$, then, equation (A1) is reduced to

$$x^{1+\alpha+\beta} \sim \frac{4\pi Q_L Y_\infty J_L}{s_e n_e h(\alpha+\beta+2)} \left(\frac{\alpha+\beta+1}{\alpha+\beta+2} \right)^{\alpha+\beta} \left(\frac{h\nu_L}{k_B T} \right)^{\alpha+\beta} \left(\frac{\pi m_e}{8k_B T} \right)^{1/2}, \quad (\text{A3})$$

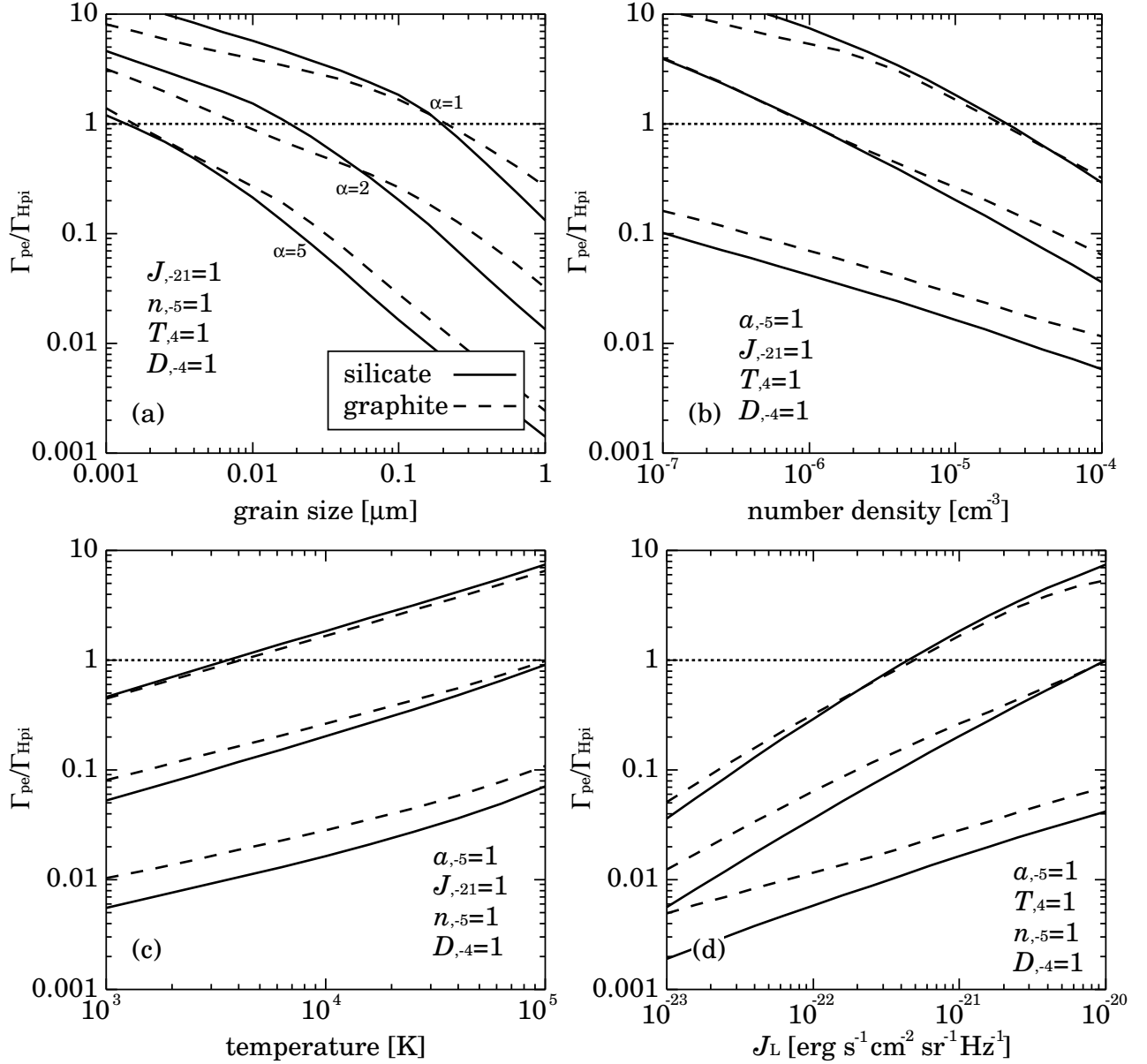


Figure A3. Ratio of dust photoelectric heating rate to hydrogen photoionization heating rate as a function of (a) grain size, (b) gas number density, (c) gas temperature, and (d) mean intensity at the Lyman limit. Notations are the same as Figure A1. Additional parameter, \mathcal{D} is the dust-to-gas mass ratio; $\mathcal{D}_{,-4} = \mathcal{D}/10^{-4}$.

where we approximated $I_p \approx x k_B T$ because $W/k_B T \sim 1$ for $T \sim 10^4$ K, and substituted $\langle v_e \rangle = (\pi m_e / 8 k_B T)^{1/2}$. Therefore, we find

$$\frac{eU}{k_B T} \propto \left(\frac{J_L Q_L(a)}{n} \right)^{1/(1+\alpha+\beta)} T^{-(1/2+\alpha+\beta)/(1+\alpha+\beta)}. \quad (\text{A4})$$

Indeed, such dependences are found in Figure A1. Moreover, $Q_L \propto a$ for $a \lesssim 0.1 \mu\text{m}$ and $Q_L \sim 1$ for otherwise. Thus, $eU/k_B T$ shows nearly no dependence of grain size for a large size.

The mean photoelectron energy is defined as

$$\langle E_{\text{pe}} \rangle = \frac{\int E_{\text{pe}} Q_{\nu} Y_{\nu} \frac{4\pi J_{\nu}}{h\nu} d\nu}{\int Q_{\nu} Y_{\nu} \frac{4\pi J_{\nu}}{h\nu} d\nu}, \quad (\text{A5})$$

where E_{pe} is the energy of the photoelectron, which is approximated to be $E_{\text{pe}} \approx (1/2)(h\nu - I_{\text{p}})$ because a part of energy of the incident photon is converted to the phonon energy of the grain (Weingartner & Draine 2001b).

If we define a function as $g(h\nu) = E_{\text{pe}} Q Y J / h\nu$ and assume the functional forms adopted above for Q , Y , and J , $\partial g / \partial h\nu$ is zero only when $h\nu = h\nu_{**} = I_{\text{p}}(\alpha + \beta + 2) / (\alpha + \beta)$. Thus, the integral in the numerator of equation (A5) is approximated to be $E_{\text{pe}}(h\nu_{**}) Q(h\nu_{**}) Y(h\nu_{**}) J(h\nu_{**})$. If $x \gg 1$, we obtain

$$\frac{\langle E_{\text{pe}} \rangle}{x k_{\text{B}} T} \sim \frac{2}{\alpha + \beta} \left(\frac{\alpha + \beta}{\alpha + \beta + 1} \right)^{\alpha + \beta}. \quad (\text{A6})$$

Therefore, $\langle E_{\text{pe}} \rangle / k_{\text{B}} T$ has a similar parameter dependence to $eU / k_{\text{B}} T$, which is observed in Figure A2.

The saturation of $\langle E_{\text{pe}} \rangle / k_{\text{B}} T$ is seen in the case of $\alpha = 1$ for a lower density in Figure A2 (b). This may be due to the effect of the maximum photon energy assumed in the calculation. We do not consider the incident photon energy higher than 1.2 keV which is the maximum energy in the data of the grain efficiency factor. For the case, I_{p} reaches several hundreds eV, so that the peak energy $h\nu_{**}$ becomes nearly the maximum energy. Thus, the above estimate may be an overestimate for such a case.

The total photoelectric heating by dust is given by $\Gamma_{\text{pe}} = n_{\text{d}} \gamma$, where n_{d} is the grain number density and γ is the heating rate per a grain. While $n_{\text{d}} \propto n a^{-3}$ for a fixed total dust mass with n being the gas number density, γ is proportional to $\langle E_{\text{pe}} \rangle a^2 n T^{1/2} x$ because the photoelectric ionization rate per a grain balances with the electron capture rate per a grain, where a^2 dependence comes from the geometrical cross section of grains. We have assumed $x \gg 1$ again. On the other hand, the photoionization heating rate, Γ_{Hpi} , is proportional to $n^2 T^{-0.7}$ in the photoionization equilibrium, where the temperature dependence comes from the recombination coefficient. Therefore, we find

$$\frac{\Gamma_{\text{pe}}}{\Gamma_{\text{Hpi}}} \propto a^{-1} x^2 T^{2.2}, \quad (\text{A7})$$

where we have used the relation $\langle E_{\text{pe}} \rangle \propto x T$ (equation [A6]). Such a dependence of J , n , or T is found in Figures A3 (b), (c), or (d), respectively. Because $Q_{\text{L}} \propto a$ for $a \lesssim 0.1 \mu\text{m}$ and $Q_{\text{L}} \sim 1$ for otherwise, we see a double power-law dependence of a in panel (a) of Figure A3.

APPENDIX B: CHEMICAL RATE EQUATIONS AND COEFFICIENTS

In this paper, we consider HI, HII, HeI, HeII, HeIII, and electron as gaseous species. That is, we neglect the effect of the metal production by stars. Thus, the primordial helium mass fraction $Y = 0.24$ is always adopted throughout our calculation.

Let us define a non-dimensional number abundance of each gaseous species as

$$X_i \equiv \frac{n_i}{n_b}, \quad (\text{B1})$$

where n_i is the number density of i -th species, and n_b is the baryon number density, which is given by $n_b(z) = \Omega_b \rho_{c,0}(1+z)^3/\mu$ with $\rho_{c,0}$ being the local critical density, and μ being the mean mass of baryon particles. Baryon is assumed to be only hydrogen and helium. Using the helium mass fraction Y , hence, we obtain

$$X_{\text{HI}} + X_{\text{HII}} = \frac{4(1-Y)}{4-3Y}, \quad (\text{B2})$$

$$X_{\text{HeI}} + X_{\text{HeII}} + X_{\text{HeIII}} = \frac{Y}{4-3Y}, \quad (\text{B3})$$

and

$$\mu = \left(\frac{4}{4-3Y} \right) m_p, \quad (\text{B4})$$

where m_p is the proton mass. For electron abundance, we have

$$X_e = X_{\text{HII}} + X_{\text{HeII}} + 2X_{\text{HeIII}}. \quad (\text{B5})$$

Chemical rate equations for the gaseous species are

$$\frac{dX_{\text{HI}}}{dt} = X_{\text{HII}}X_en_b\alpha_{\text{HII}} - X_{\text{HI}}(X_en_b\beta_{\text{HI}} + \gamma_{\text{HI}}), \quad (\text{B6})$$

$$\frac{dX_{\text{HeI}}}{dt} = X_{\text{HeII}}X_en_b\alpha_{\text{HeII}} - X_{\text{HeI}}(X_en_b\beta_{\text{HeI}} + \gamma_{\text{HeI}}), \quad (\text{B7})$$

and

$$\frac{dX_{\text{HeIII}}}{dt} = -X_{\text{HeIII}}X_en_b\alpha_{\text{HeIII}} + X_{\text{HeII}}(X_en_b\beta_{\text{HeII}} + \gamma_{\text{HeII}}), \quad (\text{B8})$$

where α_i , β_i , and γ_i are recombination coefficients, collisional ionization coefficients, and photoionization rates for i -th species, respectively. The adopted functions of α_i and β_i are tabulated in Table B1. The photoionization rate is given by

$$\gamma_i = \int_{\nu_i}^{\nu_{\text{max}}} \sigma_{i,\nu} \frac{4\pi J_\nu}{h\nu} d\nu \approx \frac{4\pi}{h} \sigma_i J_L \left(\frac{\nu_L}{\nu_i} \right)^\alpha \left(\frac{b_i}{\alpha + s_i} - \frac{b_i - 1}{\alpha + s_i + 1} \right), \quad (\text{B9})$$

where $J_\nu = J_L(\nu/\nu_L)^{-\alpha}$ with ν_L is the hydrogen Lyman limit frequency, and $\sigma_{i,\nu}$ is the ionization cross section:

Table B1. Recombination and collisional ionization coefficients in $\text{cm}^3 \text{s}^{-1}$ taken from Cen (1992) and Theuns et al. (1998).

Recombination	
$\alpha_{\text{HII}} = 6.30 \times 10^{-11} T^{-1/2} T_3^{-0.2} / (1 + T_6^{0.7})$	
$\alpha_{\text{HeII}} = 1.50 \times 10^{-10} T^{-0.6353} + \alpha_{\text{HeII}}^{\text{D}}$	
$\alpha_{\text{HeIII}} = 3.36 \times 10^{-10} T^{-1/2} T_3^{-0.2} / (1 + T_6^{0.7})$	
Dielectric recombination	
$\alpha_{\text{HeII}}^{\text{D}} = 1.9 \times 10^{-3} T^{-1.5} e^{-4.7 \times 10^5 / T} (1 + 0.3 e^{-9.4 \times 10^4 / T})$	
Collisional ionization	
$\beta_{\text{HI}} = 5.85 \times 10^{-11} T^{1/2} (1 + T_5^{1/2})^{-1} e^{-157809.1 / T}$	
$\beta_{\text{HeI}} = 2.38 \times 10^{-11} T^{1/2} (1 + T_5^{1/2})^{-1} e^{-285335.4 / T}$	
$\beta_{\text{HeII}} = 5.68 \times 10^{-12} T^{1/2} (1 + T_5^{1/2})^{-1} e^{-631515 / T}$	

Table B2. Parameters for ionization cross sections from Osterbrock (1989).

species	$\sigma_i [10^{-18} \text{ cm}^2]$	$\nu_i [10^{15} \text{ Hz}]$	b_i	s_i
HI	6.30	3.29	1.34	2.99
HeI	7.83	5.94	1.66	2.05
HeII	1.58	1.32	1.34	2.99

$$\sigma_{i,\nu} = \sigma_i \left[b_i \left(\frac{\nu}{\nu_i} \right)^{-s_i} + (1 - b_i) \left(\frac{\nu}{\nu_i} \right)^{-s_i-1} \right], \quad (\text{B10})$$

for $\nu \geq \nu_i$ and otherwise $\sigma_{i,\nu} = 0$ (Osterbrock 1989). The parameters for ionization cross sections are summarised in Table B2. The last term in equation (B9) is valid when $\nu_{\text{max}} \gg \nu_i$. In this paper, we set $h\nu_{\text{max}} = 1.2 \text{ keV}$.

By solving equations (B6)–(B8), we obtain X_{HI} , X_{HeI} , and X_{HeIII} . Once these fractional abundances are obtained, other abundances are found from equations (B2), (B3), and (B5). In addition, the numbers of hydrogen and helium nuclei are constant since the helium mass fraction Y is now constant. Thus, $dX_{\text{HII}}/dt = -dX_{\text{HI}}/dt$ and $dX_{\text{HeII}}/dt = -dX_{\text{HeI}}/dt - dX_{\text{HeIII}}/dt$. Therefore, the term of dX/dt in equation (6) of section 4.1 is reduced to $-dX_{\text{HI}}/dt - dX_{\text{HeI}}/dt + dX_{\text{HeIII}}/dt$ because of $dX/dt = \sum_i dX_i/dt = dX_e/dt$ and equation (B5).

We now consider the atomic photoionization heating and the photoelectric heating by dust as the heating mechanism of gas in equation (6). The photoionization heating rate per a i -th species atom/ion is given by

$$\epsilon_i = \int_{\nu_i}^{\nu_{\text{max}}} (h\nu - h\nu_i) \sigma_{i,\nu} \frac{4\pi J_\nu}{h\nu} d\nu \approx 4\pi \sigma_i \nu_i J_L \left(\frac{\nu_L}{\nu_i} \right)^\alpha \left(\frac{b_i}{\alpha + s_i - 1} - \frac{2b_i - 1}{\alpha + s_i} + \frac{b_i - 1}{\alpha + s_i + 1} \right), \quad (\text{B11})$$

where parameters, σ_i , ν_i , b_i , and s_i are summarised in Table B2, and α is the power-law spectral index of the incident radiation. Again, the last term of equation (B11) is valid when $\nu_{\text{max}} \gg \nu_i$. The dust photoelectric heating is given by calculating the equilibrium charge and the ejection rate of the photoelectron by the manner described in, for exam-

Table B3. Cooling coefficients in $\text{erg cm}^3 \text{s}^{-1}$ taken from Cen (1992) and Theuns et al. (1998).

Recombination cooling	
HII	$8.70 \times 10^{-27} T^{1/2} T_3^{-0.2} / (1 + T_6^{0.7}) X_e X_{\text{HII}}$
HeII	$1.55 \times 10^{-26} T^{0.3647} X_e X_{\text{HeII}}$
HeIII	$3.48 \times 10^{-26} T^{1/2} T_3^{-0.2} / (1 + T_6^{0.7}) X_e X_{\text{HeIII}}$
dust ^a	$(3/2) k_B T R_e n_d / n_b^2$
Dielectric recombination cooling	
HeII	$1.24 \times 10^{-13} T^{-1.5} e^{-4.7 \times 10^5 / T} (1 + 0.3 e^{-9.4 \times 10^4 / T}) X_e X_{\text{HeII}}$
Collisional ionization cooling	
HI	$1.27 \times 10^{-21} T^{1/2} (1 + T_5^{1/2})^{-1} e^{-157809.1/T} X_e X_{\text{HI}}$
HeI	$9.38 \times 10^{-22} T^{1/2} (1 + T_5^{1/2})^{-1} e^{-285335.4/T} X_e X_{\text{HeI}}$
HeII	$4.95 \times 10^{-22} T^{1/2} (1 + T_5^{1/2})^{-1} e^{-631515/T} X_e X_{\text{HeII}}$
Collisional excitation cooling	
HI	$7.5 \times 10^{-19} (1 + T_5^{1/2})^{-1} e^{-118348/T} X_e X_{\text{HI}}$
HeII	$5.54 \times 10^{-17} T^{-0.397} (1 + T_5^{1/2})^{-1} e^{-47638/T} X_e X_{\text{HeII}}$
Bremsstrahlung cooling	
ion ^b	$1.42 \times 10^{-27} g_f T^{1/2} X_e (X_{\text{HII}} + X_{\text{HeII}} + 4X_{\text{HeIII}})$
Inverse compton cooling	
CMB photon ^c	$5.406 \times 10^{-36} [T - T_{\text{CMB}}(1+z)](1+z)^4 X_e / n_b$

^a R_e is the electron capture rate per a grain and n_d is the grain number density. These quantities are calculated by the way described in Inoue & Kamaya (2003).

^b g_f is the Gaunt factor and assumed to be 1.5.

^c T_{CMB} is the current temperature of the cosmic microwave background and set to be 2.7 K.

ple, Inoue & Kamaya (2003). Finally, the adopted cooling rates are summarised in Table B3. The metallic line cooling is not so important for our problem because the temperature interested is less than 25,000 K and the metallicity is 1/10–1/100 of the Solar value (Sutherland & Dopita 1993).